

## Article

# A Comparison between Solution-Based Synthesis Methods of ZrO<sub>2</sub> Nanomaterials for Energy Storage Applications

Maria Leonor Matias <sup>1</sup>, Emanuel Carlos <sup>1,\*</sup>, Rita Branquinho <sup>1</sup>, Hadassa do Valle <sup>1</sup>, João Marcelino <sup>1</sup>, Maria Morais <sup>1</sup>, Ana Pimentel <sup>1</sup>, Joana Rodrigues <sup>2</sup>, Teresa Monteiro <sup>2</sup>, Elvira Fortunato <sup>1</sup>, Rodrigo Martins <sup>1,\*</sup> and Daniela Nunes <sup>1,\*</sup>

<sup>1</sup> CENIMAT I3N, Department of Materials Science, School of Science and Technology, NOVA University Lisbon and CEMOP/UNINOVA, 2829-516 Caparica, Portugal

<sup>2</sup> Physics Department & I3N, Aveiro University, Campus Universitário de Santiago, 3810-193 Aveiro, Portugal

\* Correspondence: e.carlos@fct.unl.pt (E.C.); rm@uninova.pt (R.M.); daniela.gomes@fct.unl.pt (D.N.); Tel.: +351-21-294-8562 (R.M. & D.N.); Fax: +351-21-294-8558 (R.M. & D.N.)

**Abstract:** The present study is focused on the synthesis of zirconium dioxide (ZrO<sub>2</sub>) nanomaterials using the hydrothermal method assisted by microwave irradiation and solution combustion synthesis. Both synthesis techniques resulted in ZrO<sub>2</sub> powders with a mixture of tetragonal and monoclinic phases. For microwave synthesis, a further calcination treatment at 800 °C for 15 min was carried out to produce nanopowders with a dominant monoclinic ZrO<sub>2</sub> phase, as attested by X-ray diffraction (XRD) and Raman spectroscopy. The thermal behavior of the ZrO<sub>2</sub> nanopowder was investigated by in situ XRD measurements. From the scanning electron microscopy (SEM) and transmission electron microscopy (TEM) images, the presence of near spherical nanoparticles was clear, and TEM confirmed the ZrO<sub>2</sub> phases that comprised the calcinated nanopowders, which include a residual tetragonal phase. The optical properties of these ZrO<sub>2</sub> nanopowders were assessed through photoluminescence (PL) and PL excitation (PLE) at room temperature (RT), revealing the presence of a broad emission band peaked in the visible spectral region, which suffers a redshift in its peak position, as well as intensity enhancement, after the calcination treatment. The powder resultant from the solution combustion synthesis was composed of plate-like structures with a micrometer size; however, ZrO<sub>2</sub> nanoparticles with different shapes were also observed. Thin films were also produced by solution combustion synthesis and deposited on silicon substrates to produce energy storage devices, i.e., ZrO<sub>2</sub> capacitors. The capacitors that were prepared from a 0.2 M zirconium nitrate-based precursor solution in 2-methoxyethanol and annealed at 350 °C exhibited an average dielectric constant ( $\kappa$ ) of  $11 \pm 0.5$  and low leakage current density of  $3.9 \pm 1.1 \times 10^{-7}$  A/cm<sup>2</sup> at 1 MV/cm. This study demonstrates the simple and cost-effective aspects of both synthesis routes to produce ZrO<sub>2</sub> nanomaterials that can be applied to energy storage devices, such as capacitors.

**Keywords:** ZrO<sub>2</sub>; nanomaterials; microwave irradiation; solution combustion; energy storage devices



**Citation:** Matias, M.L.; Carlos, E.; Branquinho, R.; do Valle, H.; Marcelino, J.; Morais, M.; Pimentel, A.; Rodrigues, J.; Monteiro, T.; Fortunato, E.; et al. A Comparison between Solution-Based Synthesis Methods of ZrO<sub>2</sub> Nanomaterials for Energy Storage Applications. *Energies* **2022**, *15*, 6452. <https://doi.org/10.3390/en15176452>

Academic Editors: Bruno Peuportier and Zsuzsa Szalay

Received: 26 July 2022

Accepted: 31 August 2022

Published: 3 September 2022

**Publisher's Note:** MDPI stays neutral with regard to jurisdictional claims in published maps and institutional affiliations.



**Copyright:** © 2022 by the authors. Licensee MDPI, Basel, Switzerland. This article is an open access article distributed under the terms and conditions of the Creative Commons Attribution (CC BY) license (<https://creativecommons.org/licenses/by/4.0/>).

## 1. Introduction

Research in nanotechnology has grown over in recent years since it opens up possibilities for the design and fabrication of novel materials, as well as flexible and smart devices at the nanometer scale [1,2]. In this regard, nanostructures based on metal oxides have been extensively studied due to their unique physical and chemical properties and great potential in a myriad of applications, including electronics, energy conversion and storage, biomedicine, catalysis and sensing [3–8].

ZrO<sub>2</sub> is a metal oxide that exhibits three crystalline phases under atmospheric pressure, depending on the synthesis route: monoclinic, which is thermodynamically the most stable form [9], tetragonal and cubic [10–12]. The cubic form of ZrO<sub>2</sub> is stable at high temperatures (usually above 2370 °C), while the tetragonal is stable within the range of 1170–2370 °C, and the monoclinic phase stabilizes below 1170 °C [4,9].

ZrO<sub>2</sub> exhibits excellent properties, such as good optical transparency in the visible and near-infrared spectral range [13,14], high thermal and chemical stabilities, mechanical strength and fracture toughness, low absorption of light, high index of refraction [15], high corrosion resistance [16], high ionic stability at high temperature, it is biocompatible [17] and presents relatively low leakage current [18] and high breakdown field [19]. Despite this, ZrO<sub>2</sub> presents a wide band gap value (theoretically estimated as ~5.42 eV for monoclinic, ~6.40 eV for tetragonal and ~5.55 eV for cubic phases [14,20,21]). The introduction of defects in its structure, for instance, through doping with cations or the reduction of particle size below a critical value, is reported to allow the stabilization of high-temperature phases (i.e., cubic and/or tetragonal phases) at RT [22,23].

Applications for this material range from ceramic industry, gas sensing, solar fuel cells and biomedical/catalytic fields to its incorporation in large-scale integrated circuits, owing to a high dielectric constant and as a gate dielectric in metal-oxide-semiconductor devices (MOS) [22,24–26]. In this regard, ZrO<sub>2</sub> has emerged as a potential alternative to replace low- $\kappa$  SiO<sub>2</sub> in electronic devices [27]. It is reported that the dielectric constant of ZrO<sub>2</sub> films ranges from  $\kappa = 20$  in the monoclinic phase to  $\kappa = 37$ – $47$  for the cubic and tetragonal phases, whereas in the case of amorphous ZrO<sub>2</sub>, the dielectric constant values are between 14 and 25 [14].

Recently ZrO<sub>2</sub>-based materials have been explored in the field of energy. Optimization of the light absorption towards sunlight in zirconia has shown enormous potential for its use in solar receivers since this refractory material possesses enhanced mechanical/thermal properties and oxidation resistance, being a competitive material to substitute the typically used silicon carbide (SiC) [28,29]. Other applications include refractory/metal production [30]. In addition, it has demonstrated high energy storage performance, for instance, by employing ferroelectric ZrO<sub>2</sub> thin films as energy storage capacitors [31] or antiferroelectric ZrO<sub>2</sub>, a material for dynamic random access memories (DRAM) [32]. Moreover, ZrO<sub>2</sub> capacitors display ultra-high power density and ultra-fast charge/discharge rates, yet their energy storage densities are relatively lower than the traditional electrical energy-storage devices, such as supercapacitors and batteries [33]. Nevertheless, these devices can play a key role in energy saving and thus reducing the carbon dioxide (CO<sub>2</sub>) footprint. When associated with renewable energy sources, capacitors can have a real impact on climate change, influencing almost all sectors of human life, including the chemical/petrochemical, automotive, textiles, wood/paper and construction sectors, whereas, for the latter, with the advent of the zero carbon buildings, it can reduce the global greenhouse gas emissions emitting buildings. The future of humanity relies on addressing the availability of using carbon-neutral energy sources and finding solutions to lower the CO<sub>2</sub> footprint, industrial residues and human contaminants with direct impact in public health and on the environment.

Most of the applications for ZrO<sub>2</sub> depend on its dimensions. It is well known that when the size of metal oxide materials is reduced to the nanoscale level, different properties are found from their bulk counterparts [34]. Novel characteristics owed to quantum size effects may occur when the cluster size is smaller than the Bohr exciton radius. Moreover, the properties of the surface start to play a relevant role that may overrule the bulk ones. Hence, the synthesis method is of paramount importance to control not only the size of ZrO<sub>2</sub> nanomaterials but also the crystalline phase, morphology and lattice defects that highly influence the physico-chemical properties of the produced nanomaterials [35].

ZrO<sub>2</sub> nanomaterials have already been obtained with different morphologies, such as thin films [14], nanoparticles [36], nanobelts [37], nanowires [38] and nanotubes [39], mainly through chemical approaches [40]. The most common methods for the synthesis of ZrO<sub>2</sub> nanostructures include co-precipitation [41], sol-gel [42] and solution combustion [35], sonochemical-assisted methods [43,44], chemical vapor deposition [45], emulsion processing routes [46,47], as well as hydrothermal [10,48] and microwave syntheses [49,50]. Lately, a continuous increase in research work has been observed related to fast continuous methods for controlling the synthesis of ZrO<sub>2</sub> nanomaterials [51–55]. Continuous hydrothermal

flow synthesis (CHFS) processes are preferred due to the possibility of tailoring and obtaining unique nanoparticle properties that cannot be achieved using more conventional batch hydrothermal or other synthesis methods. These processes have shown potential in manufacturing reproducible and homogeneous nanomaterials, with high throughput, in addition to being energy efficient and eco-friendly, since for this last case, water is typically used rather than toxic organic solvents. Annealing treatments can also be avoided by employing these processes with superheated water conditions (typically in the range of 200–400 °C) [55–57]. Even though these systems offer several benefits, their high cost is a downside [57].

Several studies have reported the production of ZrO<sub>2</sub> nanomaterials using sol-gel, particularly solution combustion synthesis, which is included in the sol-gel method [58–60]. Solution combustion synthesis is an attractive technique for the preparation of ZrO<sub>2</sub> nanopowders and thin films, owing to its simplicity, energy and time savings, cost-effectiveness, versatility, higher purity compared with conventional sol-gel methods, low synthesis temperatures, and compatibility with flexible substrates and large scale production [61–63].

The synthesis of ZrO<sub>2</sub> nanomaterials using the hydrothermal method assisted by microwave irradiation has also been growing exponentially over recent years [49,64–66], mainly due to its several advantages, such as volumetric heating (the entire volume of solution is evenly heated, instead of relying on heat diffusion processes across the reaction vessels), and the reaction times can be shorter as it is possible to synthesize nanostructures in just a few minutes. Furthermore, it also allows accurate control of particle morphology and size by adjusting the microwave parameters [50,67]. Upon optimization of the synthesis parameters, such as temperature, pH, time and zirconium oxide precursors (e.g., zirconyl chloride, zirconyl hydroxide, zirconyl nitrate hydrate and zirconium alkoxides), different ZrO<sub>2</sub> phases can be obtained [68].

Solution-based ZrO<sub>2</sub> nanomaterials are a highly appealing alternative to physical methods due to their process simplicity, high throughput, reduced equipment cost, since no vacuum-based systems are required [69,70], and the possibility to fabricate optoelectronic devices, even at low temperatures and by using green solvents [70]. As indicated, a broad range of solution-based synthesis methods have been developed to prepare ZrO<sub>2</sub> nanomaterials; however, solution combustion synthesis and hydrothermal synthesis/microwave irradiation are typically preferred, and for that reason, these techniques are presented in this work. The same zirconium precursor (zirconium (IV) oxynitrate hydrate) was used in both synthesis techniques.

Several studies have already reported the dielectric properties of the ZrO<sub>x</sub> films produced by different solution-based processes. For instance, Seon et al. fabricated ZrO<sub>2</sub> films via a non-hydrolytic sol-gel route at low temperatures, using 2-methoxyethanol (2-ME) as a solvent, with further annealing at 300 °C. The solution precursors chosen were zirconium chloride and zirconium isopropoxide, which were prepared in equimolar amounts, and acted, respectively, as a metal halide and a metal alkoxide. A breakdown voltage greater than 4 MV cm<sup>-1</sup>, a high dielectric constant (near 10) and a low leakage current density of 5 × 10<sup>-8</sup> A cm<sup>-2</sup> at a field of 1 MV cm<sup>-1</sup> were obtained [71]. Another study by Gong et al. showed that by employing a low-temperature annealing treatment at 160 °C, high-quality amorphous ZrO<sub>2</sub> dielectric films could be produced via a low-cost solution process. In this study, a solution was prepared using zirconium (IV) acetylacetonate as zirconium precursor and N, N-dimethylformamide as a solvent. Hydrolysis and condensation reactions occurred during stirring of the solution for 32 h at 90 °C. The films exhibited a leakage current of 3.6 × 10<sup>-5</sup> A cm<sup>-2</sup> at -3 V, a capacitance of ~117.1 nF cm<sup>-2</sup> and a dielectric constant of 7.8, both at 1 KHz [72]. Wang et al. also fabricated high-κ ZrO<sub>2</sub>-dielectric films using a lightwave (LW) irradiation-induced chloride-based low-temperature solution route. Results demonstrated a great capacitance of 270 nF cm<sup>-2</sup>, a high dielectric constant of 14.1 (at 100 Hz) and a low leakage current of 7.6 × 10<sup>-8</sup> A cm<sup>-2</sup>, under 2 MV/cm. The superior performance was attributed to the effective formation of the metal-oxygen (M-O) framework that enabled the elimination of oxygen defects [73]. Another study by Jung et al.

demonstrated the fabrication of ultrathin  $ZrO_x$  films by deep ultraviolet irradiation, which revealed a leakage current density as low as  $10^{-11}$  A  $cm^{-2}$  at 1 MV/cm, a capacitance of 260 nF  $cm^{-2}$  (at 1 MHz), high dielectric constant (22) and good breakdown voltage (around 6 MV/cm) [74]. In addition, Luo et al. prepared high-quality  $ZrO_2$  films using an oxygen-doped precursor solution (ODS). The ODS- $ZrO_2$  films showed a low leakage current density of  $10^{-7}$  A  $cm^{-2}$  (at 2 MV/cm), high breakdown electric field (7.0 MV/cm) and dielectric constant of 19.5 [75]. However, the challenge still relies on the fabrication of metal-oxide films with a high-quality surface (a smooth surface with a dense network) at a low temperature and through a simple approach to guarantee a low leakage current density and high breakdown field [75].

In this study,  $ZrO_2$  nanomaterials were produced in the form of powders or thin films through solution-based processes, i.e., a hydrothermal method assisted by microwave irradiation and solution combustion synthesis. The microwave synthesized powder was further calcinated at 800 °C for 15 min under atmospheric conditions. The  $ZrO_2$  nanomaterials were characterized by XRD, Raman spectroscopy, SEM coupled with energy dispersive X-ray spectroscopy (EDS) and focused ion beam (FIB) and TEM. The thermal behavior of the nanopowder produced under microwave irradiation was investigated through in situ XRD, and these powders had their optical properties assessed through PL and PLE at RT. The  $ZrO_x$  thin films produced by the solution combustion synthesis were further tested as capacitors.

## 2. Materials and Methods

### 2.1. Hydrothermal Synthesis of $ZrO_2$ Nanoparticles Assisted by Microwave Irradiation

The  $ZrO_2$  nanoparticle synthesis route was adapted from ref. [4]. In a typical synthesis, 50 mL of an aqueous (aq.) solution of 0.2 M of zirconium (IV) oxynitrate hydrate (Sigma-Aldrich, St. Louis, MO, USA, 99.9%, CAS: 14985-18-3,  $ZrO(NO_3)_2 \cdot xH_2O$ ) is mixed with 50 mL of an aq. solution of 0.4 M of sodium hydroxide (Labchem, CAS: 1310-73-2, NaOH). The reagents were used without any further purification. The 100 mL solution was left to stir for 30 min. The molar ratio of zirconium precursor and sodium hydroxide was kept at 1:2. Microwave synthesis was then carried out with a CEM microwave digestion system, Matthews, NC, USA (MARS one), and the applied microwave parameters were 1000 W,  $230 \pm 10$  °C and 25 min. Afterwards, the previous solution was equally distributed into Teflon vessels of 75 mL (each vessel containing 20 mL of solution). Subsequently, the centrifugation of the resultant nanopowder was performed for 3 min at 4750 rpm and washed three times alternately with deionized water and isopropyl alcohol (IPA). Finally, the nanopowder was dried in a desiccator at 60 °C for 5 h. The yield was around 0.77 g of nanopowder/batch.

After microwave synthesis, the dried  $ZrO_2$  nanopowder was further calcinated in an alumina ceramic crucible at 800 °C for 15 min using a Nabertherm furnace under atmospheric conditions. The calcination treatment aimed to guarantee the formation of the mostly thermodynamically stable  $ZrO_2$  phase, i.e., the monoclinic phase.

### 2.2. Solution Combustion Synthesis

A solution with a concentration of 0.2 M of zirconium (IV) oxynitrate hydrate (Sigma-Aldrich, 99.9%, CAS: 14985-18-3) was prepared in 2-methoxyethanol (2-ME, ACROS Organics, 99%,  $C_3H_8O_2$ ), and it was left to stir at room temperature for 2 h. Urea (Sigma-Aldrich, 98%,  $CO(NH_2)_2$ ) was used as fuel for the combustion reaction and continued stirring for a minimum of 1 h. The molar proportion between urea and the zirconium oxide precursor was 5:3 to ensure the redox stoichiometry of the reaction. The powder was produced considering 10 mL of the combustion solution with the same concentration and transferred to an alumina ceramic crucible for further annealing in an air furnace at 350 °C for 1 h.

As for the thin films, and prior to the  $ZrO_x$  deposition, a  $2.5 \times 2.5$  cm *p*-type single crystal 100-oriented silicon substrate (resistivity  $\cong 1\text{--}2$   $\Omega$ -cm) was cleaned with acetone for 10 min in an ultrasonic cleaning bath at 60 °C. This cleaning process was repeated with

IPA, followed by deionized water and then the substrates were dried using nitrogen flow. The adhesion properties of the thin films to the substrate were enhanced by exposing the substrate to UV-ozone treatment (PSD-UV Novascan system-Ames, IA, USA) for 15 min at a 5 cm distance from the UV lamp. Prior to solution casting, the precursor solution was filtered through a 0.22  $\mu\text{m}$  polytetrafluoroethylene (PTFE) syringe filter and one layer was deposited by spin coating on the silicon (Si) substrate at 2000 rpm for 35 s. To evaporate the solvent and improve the densification, the thin films were later annealed at 350  $^{\circ}\text{C}$  on a hot plate for 30 min.

The metal-insulator-semiconductor (MIS) capacitors were fabricated considering the structure  $\text{Al}/\text{ZrO}_x/p\text{-Si}$ . The schematic of the MIS devices' fabrication is depicted in Figure 1. To optimize the ohmic contact, the capacitors were completed by thermal evaporation of an 80 nm aluminum bottom electrode on the Si substrate and 80 nm Al top electrodes by applying a circular shadow mask, which produced capacitors with an area of 0.2  $\text{mm}^2$ .

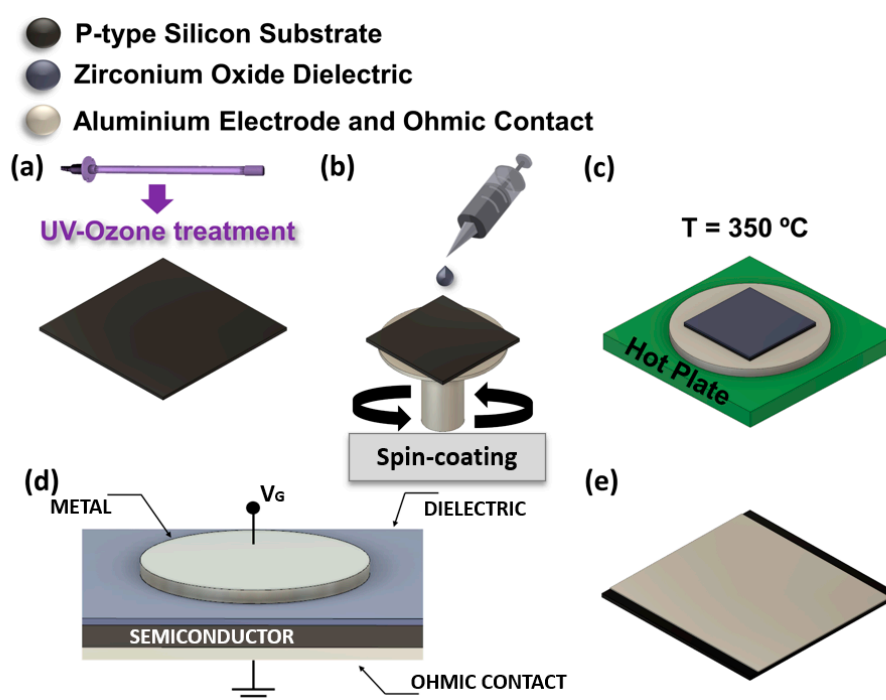


**Figure 1.** Steps to fabricate the MIS capacitor after the cleaning procedure: (a) surface treatment on silicon (Si) substrate by UV-ozone for 15 min; (b) deposition of the zirconium oxide precursor solution by spin coating technique; (c) annealing treatment of the substrate for film densification; (d) scheme of the device after the deposition of top electrodes (80 nm Al) by thermal evaporation; (e) scheme of the device after the deposition of the bottom electrode (80 nm Al) by thermal evaporation.

### 2.3. Characterization Techniques

XRD experiments were carried out using a PANalytical's X'Pert PRO MPD diffractometer (Almelo, The Netherlands) equipped with an X'Celerator 1D detector and using  $\text{CuK}\alpha$  radiation ( $\lambda = 1.540598 \text{ \AA}$ ). XRD data were recorded from 20 $^{\circ}$  to 80 $^{\circ}$  2 $\theta$  range with a step of 0.05 $^{\circ}$ . The produced  $\text{ZrO}_2$  nanopowders were measured in the Bragg–Brentano configuration. The crystalline phases in the produced nanopowders were identified by comparison with the International Centre for Diffraction Data (ICDD). The simulated monoclinic phase corresponds to ICDD file No. 00-037-1484, the simulated tetragonal phase to ICDD file No. 00-050-1089 and the simulated cubic phase to ICDD file No. 00-049-1642. In situ XRD experiments were performed in an MRI chamber from Bruker (Massachusetts, United States of America) at atmospheric conditions using a Pt–Rh foil as the heating element. The in situ diffractograms were recorded in the same 2 $\theta$  range (20 $^{\circ}$  to 80 $^{\circ}$ ) at temperatures of 30, 100, 200, 300, 400, 500, 600, 700 and 800  $^{\circ}\text{C}$ . The  $\text{ZrO}_2$  nanopowder was

kept at each temperature for 15 min, during which 15 consecutive scans were performed between 27° and 33° with a scanning step of 0.017° to investigate the evolution of the monoclinic and tetragonal phases. The temperature was increased at a rate of 50 °C/min.

The crystallinity of the produced ZrO<sub>x</sub> thin films on silicon substrates annealed at 350 °C was also investigated using the same XRD equipment in grazing incidence mode (GIXRD, X'Pert PRO PANalytical) with a step of 0.2°/min and an angle of incidence of the X-ray beam fixed at 0.5° in the range of 10–60° (2θ).

SEM images were acquired using a Hitachi Regulus 8220 Scanning Electron Microscope (Mito, Japan) equipped with energy dispersive X-ray spectroscopy (EDS) equipment. For the FIB experiments, a Carl Zeiss AURIGA CrossBeam (FIB-SEM) workstation (Carl Zeiss MicrosPANI/TiO<sub>2</sub> copy GmbH, Oberkochen, Germany) was used. The inner structure of the ZrO<sub>2</sub> capacitor was observed by FIB, where Ga<sup>+</sup> ions were accelerated to 30 kV at 50 pA, and the etching depth was maintained at around 500 nm. TEM observations were performed with a Hitachi HF5000 field-emission transmission electron microscope (Mito, Japan) operated at 200 kV. A drop of the sonicated dispersions was deposited onto 200-mesh lacey-carbon copper grids and allowed to dry before observation. The average particle size and standard deviation were calculated from the dimensions of 50 nanoparticles with ImageJ software based on TEM images.

Raman spectroscopy measurements were conducted with an inVia Qontor confocal Raman microscope from Renishaw (Kingswood, UK). A 50 mW green diode operated at 532 nm was used as the excitation source, with an exposure time of 10 s and settings of 3 and 7 accumulations for ZrO<sub>2</sub> nanopowders before and after annealing treatment, respectively. The laser beam was focused with a long working distance (8.2 mm) 50 × Olympus objective and a 100 × Olympus objective with 0.35 mm working distance, respectively, for the samples before and after annealing treatment. The Raman spectra were recorded in the range of 110–800 cm<sup>-1</sup> (as an extended scan). Several scans on different points of the ZrO<sub>2</sub> nanopowder's surface were recorded, and the present results are based on their average. Possible fluctuations of the Raman equipment were avoided with a previous calibration with a silicon wafer (521 cm<sup>-1</sup> peak). All Raman measurements were performed at ambient conditions.

RT PL and PLE measurements were carried out in the microwave synthesized ZrO<sub>2</sub> nanopowders, before and after calcination, using a Fluorolog-3 Horiba Scientific set-up with a double additive grating Gemini 180 monochromator (1200 gr/mm and 2 × 180 mm) in the excitation and a triple grating iHR550 spectrometer in the emission (1200 gr/mm and 550 mm). A 450 W Xe lamp was used as the excitation source, and different excitation wavelengths were explored. The PLE data was obtained by monitoring the maximum of the PL emission.

The electrical and dielectric properties such as capacitance-voltage ( $C - V$ ), capacitance-frequency ( $C - f$ ) and current-voltage ( $I - V$ ) measurements of the MIS capacitors ZrO<sub>x</sub>-based were investigated by using a semiconductor parameter analyzer (Keysight B1500A) with a probe station (Cascade EPS150 Triax).

### 3. Results and Discussion

#### 3.1. Structural and Optical Characterization of the ZrO<sub>2</sub> Nanopowders Produced under Microwave Irradiation

##### 3.1.1. Raman Spectroscopy Measurements

ZrO<sub>2</sub> nanopowder was synthesized through a hydrothermal method assisted by microwave irradiation. Raman spectroscopy measurements were performed to investigate the crystalline phase of the synthesized ZrO<sub>2</sub> nanoparticles [76]. A further calcination process was also carried out at 800 °C for 15 min. Figure 2a,b show the Raman spectra in the 110–800 cm<sup>-1</sup> range for the synthesized ZrO<sub>2</sub> nanopowders before and after the calcination treatment, respectively. Regarding the as-synthesized ZrO<sub>2</sub> powder, as seen in Figure 2a, broader Raman bands were observed when a comparison was made with the calcinated material (Figure 2b) [77]. Nevertheless, some of the peak positions of the

vibrational modes occurred at the same frequencies, meaning that contributions of the same ZrO<sub>2</sub> polymorph were present in both materials. Tetragonal zirconia (D<sub>4h</sub> point group) was expected to exhibit six Raman active vibrational modes at the  $\Gamma$  point of the first Brillouin zone with A<sub>1g</sub> + 2B<sub>1g</sub> + 3E<sub>g</sub> symmetries [78]. The frequencies of these modes were reported as 146 cm<sup>-1</sup> (E<sub>g</sub>), 270 cm<sup>-1</sup> (A<sub>1g</sub>), 318 cm<sup>-1</sup> (B<sub>1g</sub>), 458 cm<sup>-1</sup> (E<sub>g</sub>), 602 cm<sup>-1</sup> (B<sub>1g</sub>) and 648 cm<sup>-1</sup> (E<sub>g</sub>) [79]. For the case of the monoclinic ZrO<sub>2</sub> (C<sub>2h</sub> point group), group theory analysis predicted 18 Raman active modes, 9A<sub>g</sub> + 9B<sub>g</sub> [80], with frequencies reported at 179 cm<sup>-1</sup> (A<sub>g</sub>), 190 cm<sup>-1</sup> (A<sub>g</sub>), 224 cm<sup>-1</sup> (B<sub>g</sub>), 305 cm<sup>-1</sup> (A<sub>g</sub>), 334 cm<sup>-1</sup> (B<sub>g</sub>), 348 cm<sup>-1</sup> (A<sub>g</sub>), 381 cm<sup>-1</sup> (B<sub>g</sub>), 476 cm<sup>-1</sup> (A<sub>g</sub>), 505 cm<sup>-1</sup> (B<sub>g</sub>), 536 cm<sup>-1</sup> (B<sub>g</sub>), 556 cm<sup>-1</sup> (A<sub>g</sub>), 616 cm<sup>-1</sup> (B<sub>g</sub>), 637 cm<sup>-1</sup> (A<sub>g</sub>) and a non-indexed peak at 757 cm<sup>-1</sup> [77,81]. By comparing the spectra of the two materials in Figure 2, we were able to identify that the vibrational modes matched those reported for both crystalline phases [77,81]. In particular, the bandwidth of the Raman lines in the as-synthesized material was likely to be due to the overlap of the vibrational signatures from the tetragonal and monoclinic ZrO<sub>2</sub>, as clearly identified by the presence of the 146 cm<sup>-1</sup> and 265 cm<sup>-1</sup> resonances and the bandshape asymmetry observed at 458 cm<sup>-1</sup> and 648 cm<sup>-1</sup>, which were assigned to the tetragonal phase. In contrast with Figure 2a, no bands related to the tetragonal ZrO<sub>2</sub> are visible in Figure 2b; however, its presence cannot be excluded. In addition, another band at 501 cm<sup>-1</sup> (B<sub>g</sub>) is visible, assigned to monoclinic ZrO<sub>2</sub> [77,81]. Cubic zirconia exhibits a characteristic broad band mode centered at 625 cm<sup>-1</sup> due to disordered oxygen sub-lattice. This vibrational mode is not visible in Figure 2a,b. Moreover, the absence of the cubic phase was already expected since it is stable only at annealing temperatures near to ZrO<sub>2</sub> melting point or at RT by doping processes [82]. No other bands were detected [83].

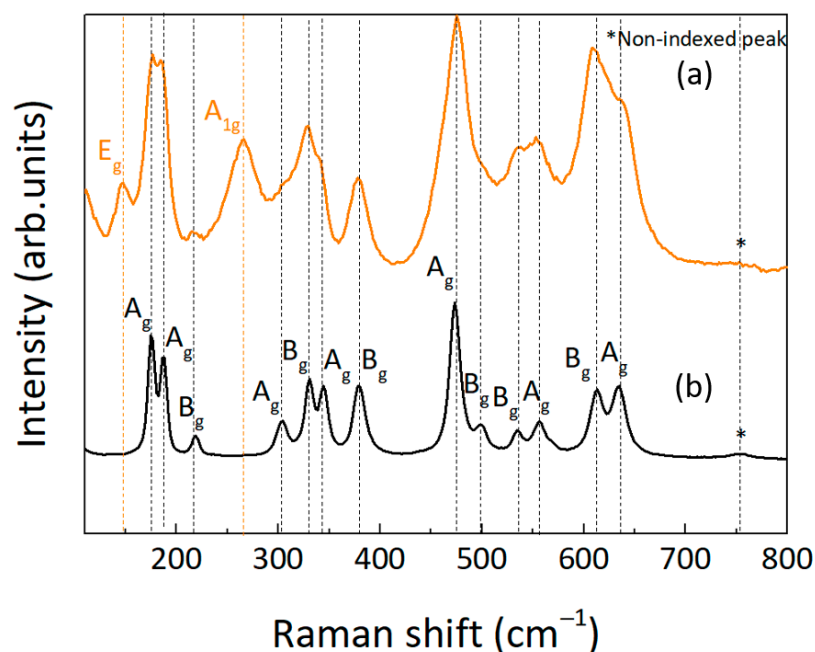


**Figure 2.** Raman spectra of the synthesized ZrO<sub>2</sub> nanopowders: (a) before and (b) after calcination at 800 °C for 15 min. The black and orange vertical dash lines represent the expected frequencies for the monoclinic and tetragonal ZrO<sub>2</sub>, respectively, and according to [77,79,81].

### 3.1.2. X-ray Diffraction

XRD measurements were also performed to confirm the crystalline phase/phases obtained from Raman spectroscopy measurements. As seen in Figure 3a, the as-synthesized ZrO<sub>2</sub> nanopowder presents a mixture of ZrO<sub>2</sub> tetragonal and monoclinic phases, considering the ICDD card numbers 00-037-1484 and 00-050-1089 for the ZrO<sub>2</sub> monoclinic and tetragonal phases, respectively.

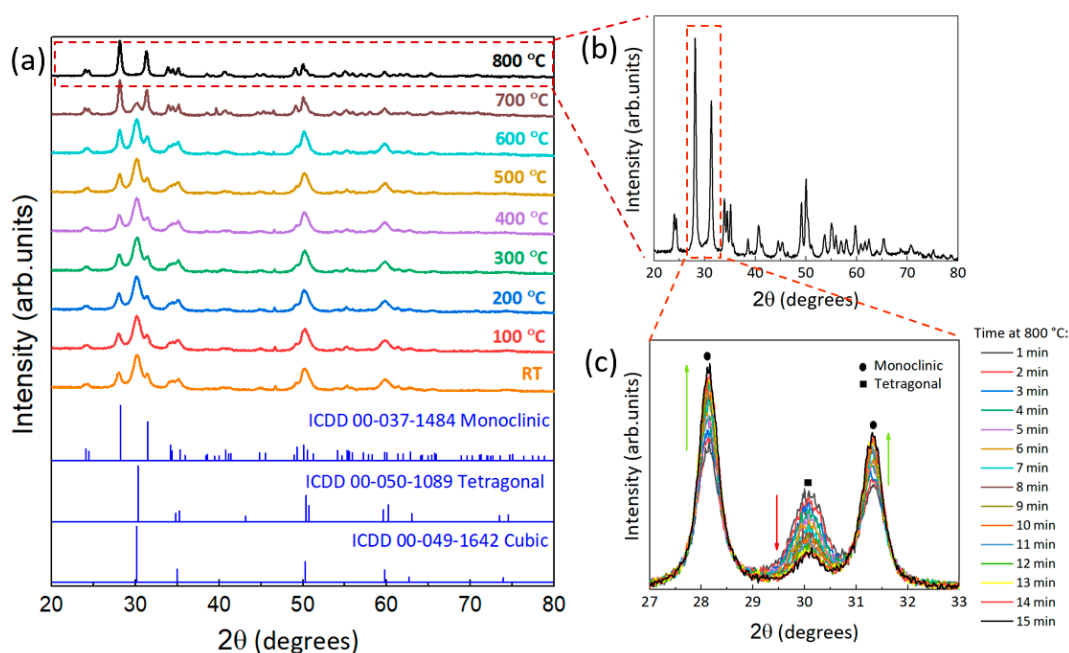


**Figure 3.** (a) In situ XRD diffractograms of the  $\text{ZrO}_2$  nanopowder synthesized under microwave irradiation with different annealing temperatures ranging from RT to  $800\text{ }^\circ\text{C}$  with a plateau time of 15 min. For comparison, the simulated monoclinic, tetragonal and cubic zirconia structures are also presented. (b) XRD diffractogram of  $\text{ZrO}_2$  nanopowder synthesized under microwave irradiation and calcinated at  $800\text{ }^\circ\text{C}$  for 15 min. (c) In situ XRD diffractograms of the  $\text{ZrO}_2$  nanopowder at  $800\text{ }^\circ\text{C}$  for different annealing times. Green arrows represent an increase of monoclinic phase, while the red arrow indicates a decrease of tetragonal phase.

Calcination treatment after microwave synthesis is an important step in transforming an amorphous to crystalline phase or a single/mixture of crystalline phases into a specific crystalline phase, inducing optical and structural modifications to the material [13,84]. In this regard, XRD diffractograms of the  $\text{ZrO}_2$  nanopowder were recorded at different temperatures to infer the thermal behavior of the  $\text{ZrO}_2$  nanomaterials and thus analyze the phase transition from tetragonal to monoclinic, Figure 3a. As can be observed, the intensity of the diffraction maximum at  $30.176^\circ$ , characteristic of the tetragonal phase, decreases with increasing temperature. At  $800\text{ }^\circ\text{C}$ , the peaks detected in the diffractogram of the  $\text{ZrO}_2$  nanopowder (Figure 3b) were fully assigned to the monoclinic  $\text{ZrO}_2$  phase (ICDD 00-037-1484). However, when performing XRD studies from  $27^\circ$  and  $33^\circ$  (Figure 3c) with a fixed temperature of  $800\text{ }^\circ\text{C}$  but different annealing times (each minute was recorded up to 15 min), it is evident that the conversion to monoclinic is accomplished at  $800\text{ }^\circ\text{C}$  with a minimal presence of the tetragonal phase. No other crystalline phases or impurities were detected with either of these two techniques.

The phase transformation of  $\text{ZrO}_2$  tetragonal to monoclinic at  $800\text{ }^\circ\text{C}$  has been previously reported in the literature. Horti et al. [13] prepared  $\text{ZrO}_2$  nanoparticles by chemical co-precipitation method and further annealed at different temperatures for 2 h, whose phase transition of tetragonal to monoclinic was seen to occur at the calcination temperature of  $800\text{ }^\circ\text{C}$ , with an evident mixture of both phases. In another study [85],  $\text{ZrO}_2$  nanoparticles were produced by conventional and ultrasound-assisted precipitation in an alkaline medium followed by calcination at different temperatures ranging from  $400\text{ }^\circ\text{C}$  to  $900\text{ }^\circ\text{C}$  for 3 h. At  $800\text{ }^\circ\text{C}$ , a mixture of three  $\text{ZrO}_2$  phases was reported, i.e., tetragonal-monoclinic-cubic phases. The present study has the advantage of having monoclinic  $\text{ZrO}_2$  as the dominant phase after a fast calcination treatment of 15 min instead of hours.

### 3.1.3. Electron Microscopy

Figure 4 shows the SEM images of the ZrO<sub>2</sub> nanoparticles synthesized under microwave irradiation with a further calcination treatment at 800 °C for 15 min. It can be seen that the particles display a nearly spherical shape (Figure 4a), and from the EDS measurements, a homogeneous distribution of Zr (Figure 4b) and O (Figure 4c) is evident. No impurities were detected by EDS.

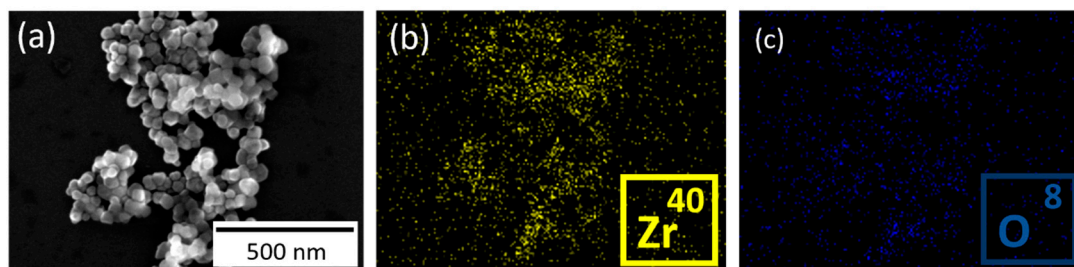


**Figure 4.** (a) SEM image of the ZrO<sub>2</sub> nanoparticles synthesized by microwave irradiation with a further calcination step at 800 °C for 15 min, together with the corresponding EDS maps of Zr (b) and O (c).

The atomic percentages (at.%) of Zr and O were also estimated from EDS spectra for the ZrO<sub>2</sub> nanopowders before and after the calcination treatment (Table 1). The atomic percentage values were close to those expected for pure zirconium oxide (the Zr/O ratio was 1:2 for the material before calcination and 1:2.7 after calcination).

**Table 1.** EDS point analysis of the ZrO<sub>2</sub> nanopowders before and after the calcination treatment at 800 °C for 15 min.

Elements	ZrO <sub>2</sub> Nanopowder before the Calcination Treatment		ZrO <sub>2</sub> Nanopowder after the Calcination Treatment	
	Zr	O	Zr	O
at.%	33.3	66.7	26.9	73.1

TEM measurements were also carried out for the ZrO<sub>2</sub> nanoparticles produced under microwave irradiation before and after calcination (Figure 5). The TEM images of the ZrO<sub>2</sub> nanoparticles before calcination demonstrate the presence of heterogeneous particles with an average particle size of  $6.7 \pm 1.9$  nm. Abnormal large particles were also observed (Figure 5a,b). In terms of particle shape, microwave synthesis resulted in different nanostructures, including nanospheres, nanosquares and irregular-shaped nanoparticles. The heterogeneity detected is consistent with the XRD and Raman spectroscopy results, where it was shown that after microwave synthesis, there was a mixture of ZrO<sub>2</sub> phases, with the presence of both tetragonal and monoclinic ZrO<sub>2</sub> phases (Figures 2a and 3a). The lattice spacing of 0.3 nm measured in Figure 5c was consistent with the d-spacing of the (101) and (011) planes of the tetragonal ZrO<sub>2</sub>. Furthermore, the fast Fourier transform (FFT) image carried out through the  $[11\bar{1}]$  zone axis, attested the existence of pure tetragonal ZrO<sub>2</sub> nanocrystals.

After calcination, as expected, an expressive growth of the ZrO<sub>2</sub> nanoparticles and the presence of uniform nanoparticles in terms of size and shape were observed (Figure 5), exhibiting a nearly spherical shape, in agreement with SEM results (Figure 4a), and displaying an average particle size of  $45.7 \pm 9.9$  nm. Figure 5e,f reveal that the measured lattice spacings of 0.32 and 0.37 nm are in good agreement with the d-spacing of the  $(\bar{1}11)$  and (011) planes of the monoclinic ZrO<sub>2</sub> phase, respectively. The FFT image captured through the  $[01\bar{1}]$  zone axis (Figure 5f) also confirmed the existence of pure monoclinic ZrO<sub>2</sub> nanocrystals. From TEM measurements, it was observed that the monoclinic ZrO<sub>2</sub>

phase prevailed for the 800 °C calcinated material; however, some minor contaminations of tetragonal nanoparticles were also observed in accordance with the in situ XRD results (Figures 3c and S1).

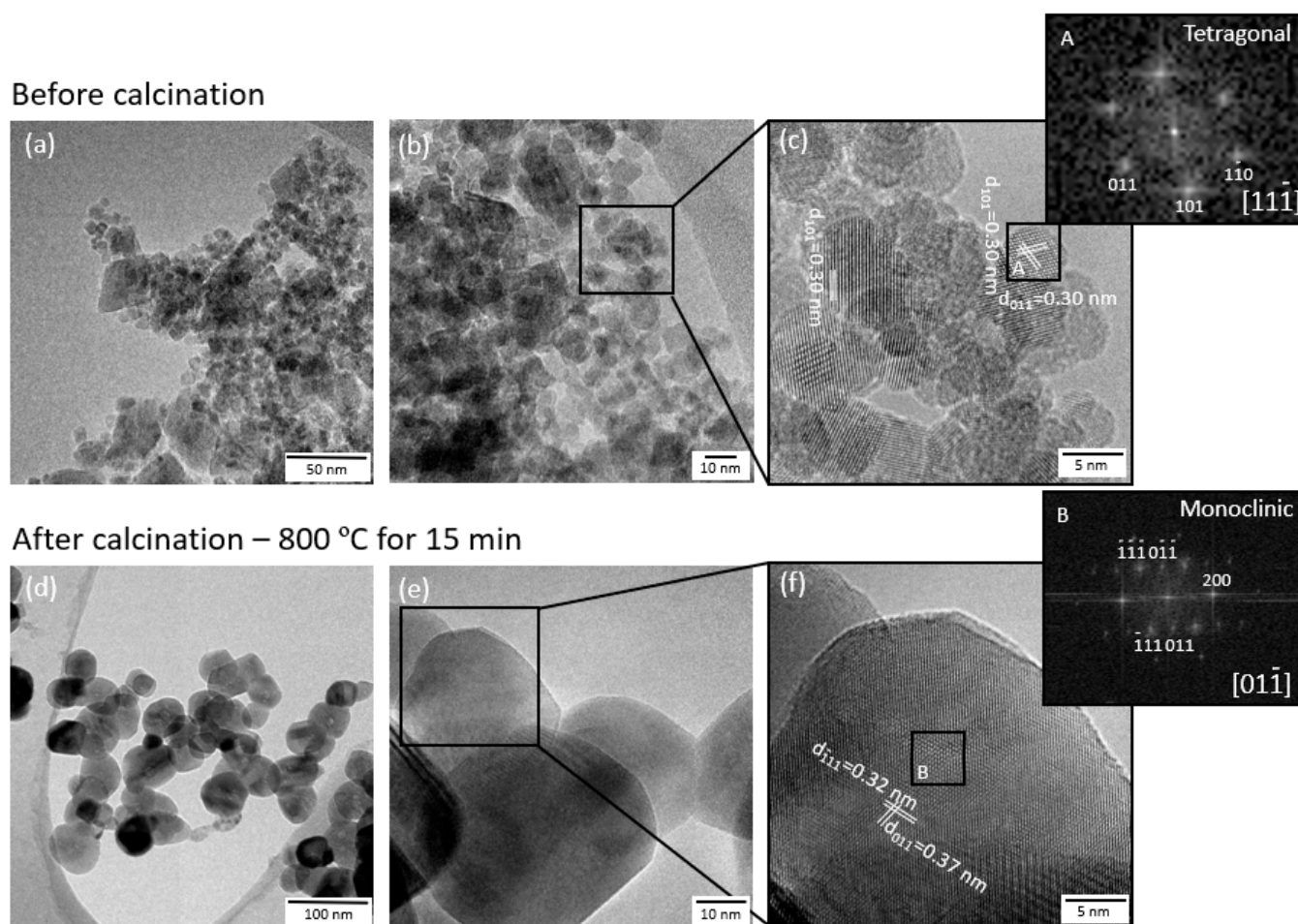


**Figure 5.** TEM images of the as-synthesized  $\text{ZrO}_2$  nanoparticles before and after calcination at 800 °C for 15 min. (a) Bright-field TEM image of the  $\text{ZrO}_2$  nanoparticles before calcination and (b) and (c) high-resolution TEM images of the  $\text{ZrO}_2$  nanocrystals. (d) Bright-field TEM image of the  $\text{ZrO}_2$  nanoparticles after calcination and (e,f) high-resolution TEM images of the  $\text{ZrO}_2$  nanocrystals. The insets in (c,f) show the FFT images of the areas (black squares) indicated as (A,B), respectively.

### 3.1.4. Photoluminescence Measurements

Figure 6 depicts the results obtained for both materials before and after calcination, with clear differences in the PL spectra. In the case of the as-synthesized nanopowder without calcination (Figure 6a), an asymmetric band was observed in the visible spectral region, with a maximum at ~415 nm (~2.99 eV) when excited with different wavelengths in the UV range. After calcination in air (Figure 6b), the visible band experienced a broadening and an increase in its intensity. Under 240 nm photon excitation, its peak position was located at ~459 nm (~2.70 eV), whereas for longer wavelengths (260–290 nm), the PL maximum shifted to longer wavelengths, around ~475 nm (~2.61 eV). Indeed, the band observed at ~459 nm is likely to be composed of several recombination channels, including the ones which are preferentially excited with photons with wavelengths in the 260–290 nm range. The PLE monitored at the maximum of the observed PL bands revealed, in both cases, an excitation band at ~310 nm (~4.00 eV), a noticed shoulder at ~260 nm (~4.77 eV) and an excitation band maximum at ~240 nm (~5.17 eV), indicating that those are the preferential population paths for the observation of such emission.

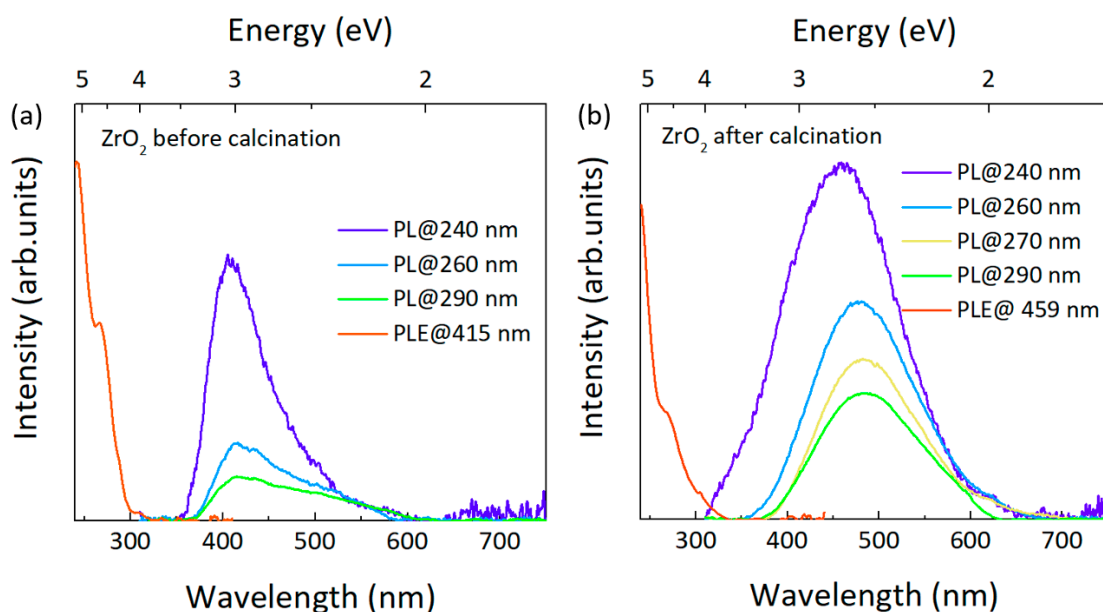


**Figure 6.** PLE/PL spectra acquired at RT on the  $\text{ZrO}_2$  nanopowders (a) before and (b) after a calcination treatment at  $800^\circ\text{C}$  for 15 min.

Broad visible bands were previously reported for the different undoped  $\text{ZrO}_2$  polymorphs, namely the monoclinic one; however, the nature of the defects that originate from them is still not fully understood [86]. Among the suggested origins, oxygen vacancies and their complexes have been pointed out as the most probable defects, even though the presence of some impurities, such as Ti, have also been proposed [86–90]. For instance, Perevalov et al. [89] studied non-stoichiometric zirconia samples prepared at different oxygen pressures and inferred that the origin of the blue emission band peaked at 2.7 eV is likely associated with charged oxygen vacancy states since a decrease of the oxygen pressure during the growth leads to an increase in the intensity of the mentioned band. Moreover, slight shifts in the peak position (between 2.6 and 2.8 eV) were seen depending on the stoichiometry of the samples. In line with the present results, the reported PLE spectra also evidence a maximum at 5.1–5.2 eV, which they associated with the optical absorption of a defect created by oxygen vacancies. Nevertheless, according to the literature, the expected band gap energy for the  $\text{ZrO}_2$  monoclinic phase predicted by theoretical models is in the range of ~5–6 eV [21,91–93], which is also in line with some experimental results [94–96]. Therefore, a likely explanation for the observed high energy excitation band that occurs in the vicinity of 240 nm (~5.17 eV) is that it corresponds to the band gap of the monoclinic  $\text{ZrO}_2$  phase, in fair agreement with the values theoretically predicted for this crystalline phase. As mentioned, the produced nanoparticles are polyphasic in nature, exhibiting a contribution of the tetragonal  $\text{ZrO}_2$  crystalline phase, which is expected to have a higher band gap energy than the monoclinic one. Therefore, the excitation shoulders/bands detected around ~260 nm and ~310 nm should be related to defects/impurities in electronic states inside the material's band gap.

Ashraf et al. [90] analyzed  $\text{ZrO}_2$  monoclinic nano- and submicron crystals annealed at different temperatures and also observed broad emission bands from ~400 nm to 600 nm, whose spectral shape and intensity slightly varied depending on the annealing conditions and crystallite sizes. The authors assigned the PL emission centered at ~482 nm (~2.57 eV) to a transition involving  $\text{F}^+$  centers, i.e., transitions from the valence band to local mid-gap states associated with singly occupied anion (oxygen) vacancies. At the shorter wavelength region, a shoulder at 422 nm (~2.94 eV) was also visible in the case of the nanoscale  $\text{ZrO}_2$  before annealing and associated with a transition to singly ionized associated oxygen vacancy defects. After annealing, this shoulder disappeared, likely related to the dissociation of those centers into  $\text{F}^+$  centers by the aid of atmospheric oxygen diffusion into the  $\text{ZrO}_2$

particles [90]. A similar phenomenon may be occurring in the present materials, explaining the redshift observed in the peak position of the band after calcination. In the case of Ashraf et al. [90], further annealing in air at higher temperatures (1500 °C) promoted additional diffusion of oxygen into the crystals, leading to a decrease in the broad band PL intensity, strengthening the assumption of the involvement of oxygen vacancy defects in the origin of this band. Their PLE spectra showed an excitation band between ~250 nm and 350 nm, which suffered a blueshift from ~300 nm (~4.13 eV) to ~280 nm (~4.43 eV) after annealing. In 2021, Loksha et al. [88] also studied monoclinic ZrO<sub>2</sub> samples, observing a broad band between 400 and 650 nm and peaked at 499 nm (~2.48 eV), which, in conjugation with other techniques, such as EPR, they attributed to the F<sup>2+</sup> center related with aggregates of the singly occupied oxygen vacancies. These broad bands are frequently deconvoluted into different components (recombination channels), which can be associated with different charged states of the vacancy-related defect [88,90,97]. As a result, the existence of distinct charge states of the F-centers can account for the fact that three excitation maxima were observed in the present samples, subsequently leading to a shift in the band peak position depending on the excitation wavelength, particularly in the case of the calcinated material. Hence, the presence of oxygen vacancy-related defects seems to be a fair hypothesis for the nature of the defects involved in the PL emission identified in the present materials.

### 3.2. Structural Characterization of the ZrO<sub>2</sub> Powder and ZrO<sub>x</sub> Thin Films Produced by Solution Combustion Synthesis

#### 3.2.1. ZrO<sub>2</sub> Powder

##### X-ray Diffraction

Solution combustion synthesis is known to produce materials in powder form but also as thin films [58,60,98]. The ZrO<sub>2</sub> powder was obtained by conventional solution combustion synthesis, with zirconium oxynitrate and urea as precursors and 2-methoxyethanol (2-ME) as a solvent. The prepared solution was further annealed in air at 350 °C for 1 h to obtain the ZrO<sub>2</sub> powder. The XRD diffractogram of the ZrO<sub>2</sub> powder is shown in Figure 7. The ZrO<sub>2</sub> tetragonal phase is clearly identified with the peak at 30.176°, associated with the (111) diffraction plane [99] (ICDD 00-050-1089), along with other diffraction maxima that were assigned to the monoclinic phase (ICDD 00-037-1484). No impurities were detected, which suggests the presence of a highly pure ZrO<sub>2</sub> powder.

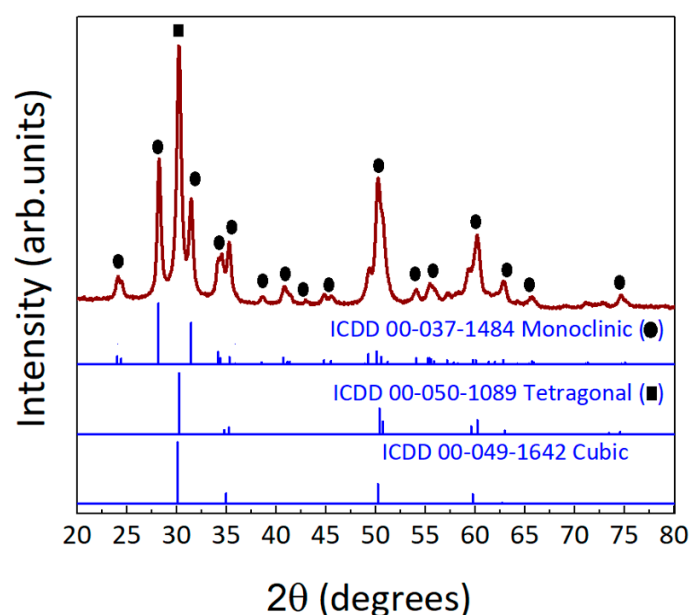


**Figure 7.** XRD diffractogram of ZrO<sub>2</sub> powder produced by solution combustion synthesis and annealed in air at 350 °C for 1 h (represented in red). For comparison, the simulated monoclinic, tetragonal and cubic zirconia structures are also presented.

### 3.2.2. Electron Microscopy

Figure 8 shows the SEM images of the  $ZrO_2$  powder resultant from the solution combustion synthesis. The formation of micro-sized plate-like structures is clear, as seen in Figure 8a. Nevertheless, Figure 8b indicates the presence of nano-sized grains composing the micro-sized structure, and Figure S2 suggests the stacking of several nanolayers. Individual nanoparticles were also observed. Moreover, the void-like nature of the particle observed in Figure S2 can be associated with the escape of gaseous combustion products that were formed during combustion synthesis [58]. EDS measurements were also carried out, and, as observed for the  $ZrO_2$  nanoparticles produced under microwave irradiation (Figure 4), the presence of a homogeneous distribution of Zr (Figure 8c) and O (Figure 8d) was clear. No impurities were detected by this technique.

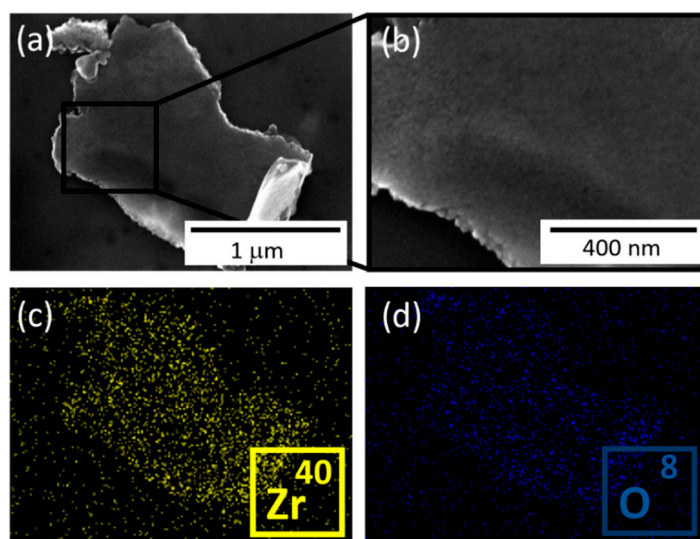


**Figure 8.** (a,b) SEM images of the  $ZrO_2$  particle produced by the combustion synthesis method and after annealing in air at 350 °C for 1 h, together with the corresponding EDS maps of Zr (c) and O (d).

The atomic percentages of Zr and O were also estimated by EDS point analysis (Table 2). As observed for the nanopowders synthesized under microwave irradiation, the values were within the expected range for pure zirconium oxide (the Zr/O ratio was 1:2.1).

**Table 2.** EDS point analysis of the  $ZrO_2$  nanopowder produced by the solution combustion synthesis.

Elements	Zr	O
at.%	31.9	68.1

The  $ZrO_2$  powder produced by solution combustion synthesis was also observed by TEM, confirming the presence of individual  $ZrO_2$  nanoparticles. From Figure 9a, nano-sized particles with different shapes can be observed, including nanospheres, nano squares and irregular-shaped nanoparticles (Figure 9a). Larger particles without a specific shape were also observed; nevertheless, the average particle size was  $10 \pm 7$  nm. The lattice spacing of 0.3 nm was measured on an individual  $ZrO_2$  nanoparticle (Figure 9b), which was consistent with the d-spacing of the (101) plane of the tetragonal  $ZrO_2$ . Nonetheless, as observed by XRD results, the powder was a mixture of tetragonal and monoclinic  $ZrO_2$  phases.

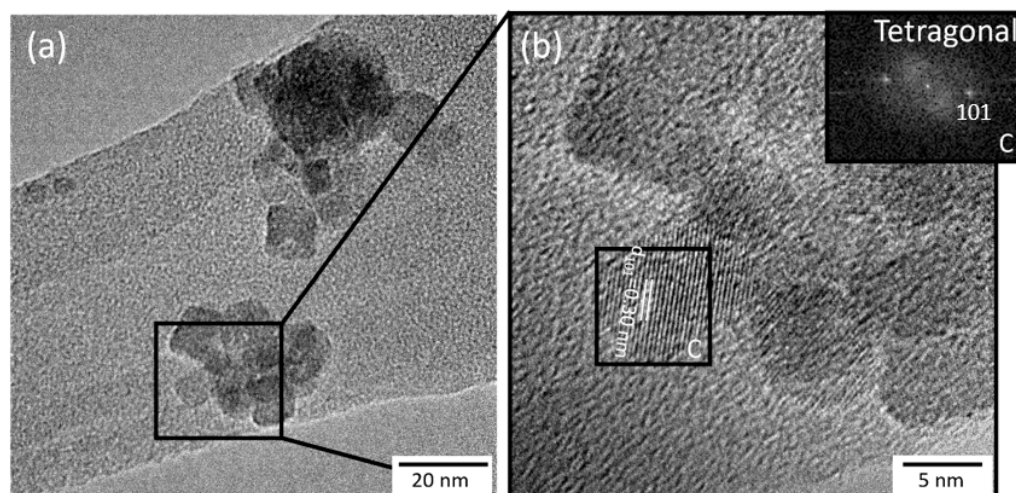


**Figure 9.** TEM images of the  $\text{ZrO}_2$  powder produced with solution combustion synthesis and annealed in air at  $350\text{ }^\circ\text{C}$  for 1 h. (a) Bright-field TEM image of the  $\text{ZrO}_2$  nanoparticles and (b) high-resolution TEM images of the  $\text{ZrO}_2$  nanocrystals. The inset in (b) shows the FFT images of the area (black square) indicated as C.

### 3.2.3. $\text{ZrO}_x$ Thin Films

#### X-ray Diffraction

The  $\text{ZrO}_x$  thin films were produced with the same solution used for producing the  $\text{ZrO}_2$  powder by solution combustion. Spin coating was employed to deposit  $\text{ZrO}_x$  thin films on silicon substrates to be tested as capacitors. Crystalline dielectric films may provide, for instance, pathways for leakage current due to the grain boundaries, which results in a small on/off ratio, leading to poor capacitor performance. On the contrary, amorphous thin films have a smooth surface, high stability, low interface state density, as well as large-area uniformity [100,101].

Grazing angle mode was performed to analyze the crystalline structure of  $\text{ZrO}_x$  thin films annealed at  $350\text{ }^\circ\text{C}$  in air for 30 min on a hot plate. An annealing treatment at  $350\text{ }^\circ\text{C}$  was carried out since it was reported that annealing treatments in solution-processed high- $\kappa$   $\text{ZrO}_x$  thin films between  $300\text{--}600\text{ }^\circ\text{C}$  are expected to increase  $\text{O}^{-2}$  content in  $\text{ZrO}_x$  films, leading to a reduction of oxygen defects and/or hydroxyl groups and consequently of conduction paths [69,102].

As observed in Figure 10, some diffraction maxima are visible at  $2\theta = 51.4^\circ$  and  $2\theta = 53.4^\circ$ , accompanied by a bump at around  $55^\circ$  ( $2\theta$ ), which correspond to forbidden diffraction planes of a (100)-oriented silicon wafer that appear when the grazing angle mode is used at certain phi angle [103]. Apart from that, no other diffraction maxima were identified, indicating the amorphous nature of the produced  $\text{ZrO}_x$  thin films, which is ideal for thin film capacitor applications.

### 3.3. Electrical Characterization of the $\text{ZrO}_x$ Capacitors

$\text{ZrO}_x$  thin films were implemented in metal-insulator-semiconductor (MIS) devices to evaluate their dielectric performance. Figure 11a show the typical C–V curve of the  $\text{ZrO}_x$  thin film capacitors with a small hysteresis. The devices present good stability with a small change of the capacitance over the frequency (1 kHz–100 kHz), as depicted in Figure 11b. To calculate the dielectric contact, a cross-section of the device to determine the  $\text{ZrO}_x$  thickness was performed, as shown in the inset of Figure 11b. The  $\text{ZrO}_x$  thin films present a capacitance per unit area of  $672 \pm 28\text{ nF cm}^{-2}$  and a dielectric constant of  $11.0 \pm 0.5$  (both calculated at 1 kHz). These values are lower when compared with vacuum deposited crystalline films due to the lower film density and presence of pores as a consequence of the solution process [71,72,104–106]. Nevertheless, the devices

present a good breakdown field of  $2.8 \pm 0.1$  MV/cm and a low leakage current density of  $(3.9 \pm 1.1) \times 10^{-7}$  A/cm<sup>2</sup> at 1 MV/cm.

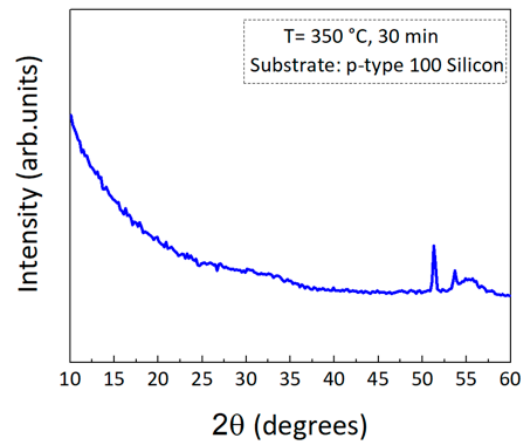


**Figure 10.** Grazing incidence XRD diffractogram of the spin-coated  $\text{ZrO}_x$  thin films annealed at  $350^\circ\text{C}$  in air for 30 min and deposited on a silicon substrate.

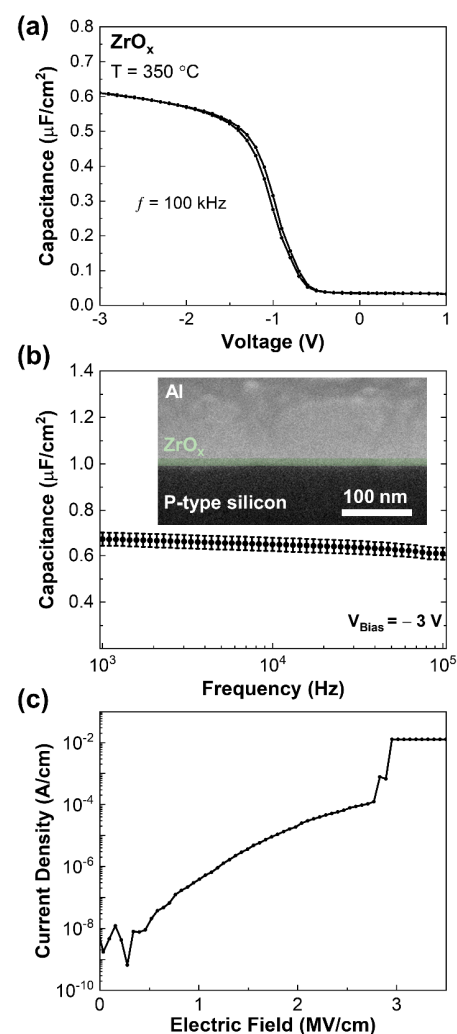


**Figure 11.** Electrical characteristics of solution-based  $\text{ZrO}_x$  MIS capacitors produced at  $350^\circ\text{C}$ : (a) typical capacitance-voltage characteristics at 100 kHz; (b) average of capacitance versus frequency characteristics, and the inset shows the cross-section SEM of the devices; (c) typical leakage current density versus the breakdown field.

Figure 11c shows a typical current density versus breakdown field dependence. The results are in accordance with solution-based  $ZrO_x$  thin film capacitors [71]. Once low leakage current density was reached ( $<10^{-5}$  A/cm<sup>2</sup>), it opens the window for future applications such as gate insulators for solution-based thin film transistors.

#### 4. Conclusions

This work demonstrated that both the hydrothermal method assisted by microwave irradiation and solution combustion synthesis are reliable and simple production routes for  $ZrO_2$  nanomaterials, including nanoparticles and thin films. Moreover, the low-cost character of the study is evidenced by the inexpensive apparatus required to produce and deposit  $ZrO_x$  thin films and thus fabricate energy storage devices. In both synthesis routes, XRD analysis revealed that the as-synthesized powders had a mixture of  $ZrO_2$  monoclinic and tetragonal phases. A calcination treatment at 800 °C for 15 min was imposed on the microwave synthesized nanopowder to promote the conversion into single-phase materials. Nevertheless, in situ XRD and TEM analysis revealed a minor presence of the  $ZrO_2$  tetragonal phase after the calcination treatment. Different nanostructures were observed after synthesis in both production routes. In the case of the microwave synthesized material, after calcination, near-spherical nanoparticles were observed, while plate-like structures composed of nano-sized grains were identified for the combustion synthesis. The effect of calcination on the optical properties of the microwave synthesized nanopowders was evaluated by PL and PLE, showing a clear broadening and an increased intensity of the  $ZrO_2$  band observed in the visible spectral region after calcination. This band was tentatively associated with the presence of oxygen vacancy-related defects. Solution combustion synthesis also resulted in thin films, and XRD analysis suggested their amorphous nature. SEM and FIB measurements of the  $ZrO_x$  capacitors revealed that the thin films present a thickness of  $14.2 \pm 0.1$  nm, which leads to a dielectric constant of  $11.0 \pm 0.5$  (calculated at 1 kHz). The devices also presented a good breakdown field of  $2.8 \pm 0.1$  MV/cm and a low leakage current density of  $(3.9 \pm 1.1) \times 10^{-7}$  A/cm<sup>2</sup> at 1 MV/cm. From this study, the production of  $ZrO_2$  nanomaterials with two simple, cost-effective and easily upscaling synthesis routes and their integration on capacitors can be highlighted.

**Supplementary Materials:** The following supporting information can be downloaded at: <https://www.mdpi.com/article/10.3390/en15176452/s1>, Figure S1: High-resolution TEM image of the  $ZrO_2$  nanocrystals calcinated at 800 °C for 15 min. The inset shows the FFT images of the area (black square) indicated as A; Figure S2: SEM image of a  $ZrO_2$  particle produced by solution combustion synthesis and annealed at 350 °C.

**Author Contributions:** M.L.M. was responsible for producing and characterizing microwave synthesized materials, as well as writing the manuscript. H.d.V. was responsible for the production and characterization of the  $ZrO_x$  films, and J.M. was responsible for the combustion powder synthesis. M.M. and A.P. were responsible for the XRD measurements. D.N., R.B. and E.C. were responsible for the overall scientific orientation and revising the manuscript. D.N. performed the TEM observations and analysis. T.M. and J.R. were responsible for the optical measurements, respective analyses and revising of the manuscript. E.F. and R.M. were responsible for supervising all the processes and obtaining funding. Part of the work resulted from the Master of Science thesis of H.d.V., titled: Effect of eco-friendly solvents in solution-based  $ZrO_x$  dielectrics, developed at the Nova School of Science and Technology. All authors have read and agreed to the published version of the manuscript.

**Funding:** This work was financed by national funds from FCT-Fundação para a Ciência e a Tecnologia, I.P., in the scope of the projects UI/BD/151292/2021 (Ph.D. research scholarship), LA/P/0037/2020, UIDP/50025/2020 and UIDB/50025/2020 of the Associate Laboratory Institute of Nanostructures, Nanomodelling and Nanofabrication-i3N, but also the 2021.03825.CEECIND. The work was also partially funded by the Nanomark collaborative project between INCM (Imprensa Nacional-Casa da Moeda) and CENIMAT/i3N. Acknowledgments also go to the EC project SYNERGY H2020-WIDESPREAD-2020-5, CSA, proposal n° 952169, EMERGE-2020-INFRAIA-2020-1, proposal n°

101008701, and to the European Community's H2020 program under grant agreement No. 787410 (ERC-2018-AdG DIGISMART).

**Data Availability Statement:** The authors confirm that the data supporting the findings of this study are available within the article and its Supplementary Materials.

**Conflicts of Interest:** The authors declare no conflict of interest.

## References

1. Shah, N.A.; Gul, M.; Abbas, M.; Amin, M. Synthesis of Metal Oxide Semiconductor Nanostructures for Gas Sensors. In *Gas Sensors*; IntechOpen: London, UK, 2019; ISBN 978-1-78985-160-1.
2. Roco, M.C.; Mirkin, C.A.; Hersam, M.C. Nanotechnology research directions for societal needs in 2020: Summary of international study. *J. Nanoparticle Res.* **2011**, *13*, 897–919. [[CrossRef](#)]
3. Chavali, M.S.; Nikolova, M.P. Metal oxide nanoparticles and their applications in nanotechnology. *SN Appl. Sci.* **2019**, *1*, 1–30. [[CrossRef](#)]
4. Ahmad, T.; Shahzad, M.; Phul, R. Hydrothermal synthesis, characterization and dielectric properties of zirconia nanoparticles. *Mater. Sci. Eng. Int. J.* **2017**, *1*, 100–104. [[CrossRef](#)]
5. Nunes, D.; Pimentel, A.; Gonçalves, A.; Pereira, S.; Branquinho, R.; Barquinha, P.; Martins, R. Metal Oxide Nanostructures for Sensor Applications. *Semicond. Sci. Technol.* **2019**, *34*, 1–178. [[CrossRef](#)]
6. Nunes, D.; Pimentel, A.; Santos, L.; Barquinha, P.; Pereira, L.; Fortunato, E.; Martins, R.; Pimentel, A.; Barquinha, P.; Pereira, L.; et al. *Metal Oxide Nanostructures: Synthesis, Properties and Applications*, 1st ed.; Korotcenkov, G., Ed.; Elsevier: Amsterdam, The Netherlands, 2018; ISBN 9780128115121.
7. Nunes, D.; Fortunato, E.; Martins, R. Flexible nanostructured TiO<sub>2</sub>-based gas and UV sensors: A review. *Discov. Mater.* **2022**, *2*, 1–23. [[CrossRef](#)]
8. Nunes, D.; Pimentel, A.; Branquinho, R.; Fortunato, E.; Martins, R. Metal oxide-based photocatalytic paper: A green alternative for environmental remediation. *Catalysts* **2021**, *11*, 504. [[CrossRef](#)]
9. Vaidya, S.; Ahmad, T.; Agarwal, S.; Ganguli, A.K. Nanocrystalline Oxalate/Carbonate Precursors of Ce and Zr and Their Decompositions to CeO<sub>2</sub> and ZrO<sub>2</sub> Nanoparticles. *J. Am. Ceram. Soc.* **2007**, *90*, 863–869. [[CrossRef](#)]
10. Behbahani, A.; Rowshanzamir, S.; Esmailifar, A. Hydrothermal Synthesis of Zirconia Nanoparticles from Commercial Zirconia. *Procedia Eng.* **2012**, *42*, 908–917. [[CrossRef](#)]
11. Van Tran, T.; Nguyen, D.T.C.; Kumar, P.S.; Din, A.T.M.; Jalil, A.A.; Vo, D.V.N. Green synthesis of ZrO<sub>2</sub> nanoparticles and nanocomposites for biomedical and environmental applications: A review. *Environ. Chem. Lett.* **2022**, *20*, 1309–1331. [[CrossRef](#)]
12. Hassan, N.S.; Jalil, A.A. A review on self-modification of zirconium dioxide nanocatalysts with enhanced visible-light-driven photodegradation of organic pollutants. *J. Hazard. Mater.* **2022**, *423 (Pt A)*, 126996. [[CrossRef](#)]
13. Liu, B.; Wang, C.; Chen, Y.; -Structural, A.; Properties of, L.Y.; Zirconia Nanopowders Korsunska, C.-C.N.; Baran, M.; Polishchuk, Y.; Horti, N.C.; Kamatagi, M.D.; et al. Structural and optical properties of zirconium oxide (ZrO<sub>2</sub>) nanoparticles: Effect of calcination temperature. *Nano Express* **2020**, *1*, 1–10. [[CrossRef](#)]
14. Boratto, M.H.; Lima, J.V.M.; Scalvi, L.V.A.; Graeff, C.F.O. Low-temperature ZrO<sub>2</sub> thin films obtained by polymeric route for electronic applications. *J. Mater. Sci. Mater. Electron.* **2020**, *31*, 16065–16072. [[CrossRef](#)]
15. Namavar, F.; Wang, G.; Cheung, C.L.; Sabirianov, R.F.; Zeng, X.C.; Mei, W.N.; Bai, J.; Brewer, J.R.; Haider, H.; Garvin, K.L. Thermal stability of nanostructurally stabilized zirconium oxide. *Nanotechnology* **2007**, *18*, 1–6. [[CrossRef](#)]
16. Abd El-Lateef, H.M.; Khalaf, M.M. Corrosion resistance of ZrO<sub>2</sub>-TiO<sub>2</sub> nanocomposite multilayer thin films coated on carbon steel in hydrochloric acid solution. *Mater. Charact.* **2015**, *108*, 29–41. [[CrossRef](#)]
17. Septawendar, R.; Sutardi, S.; Karsono, U.; Sofiyarningsih, N. A Low-Cost, Facile Method on Production of Nano Zirconia and Silica from Local Zircon in a Large Scale Using a Sodium Carbonate Sintering Technology. *J. Aust. Ceram. Soc.* **2016**, *52*, 92–102.
18. Xifeng, L.; Enlong, X.; Jianhua, Z. Low-temperature solution-processed zirconium oxide gate insulators for thin-film transistors. *IEEE Trans. Electron Devices* **2013**, *60*, 3413–3416. [[CrossRef](#)]
19. Chang, J.P.; Lin, Y.S. Dielectric property and conduction mechanism of ultrathin zirconium oxide films. *Appl. Phys. Lett.* **2001**, *79*, 3666. [[CrossRef](#)]
20. Zandiehnam, F.; Murray, R.A.; Ching, W.Y. Electronic structures of three phases of zirconium oxide. *Physica B+C* **1988**, *150*, 19–24. [[CrossRef](#)]
21. Králik, B.; Chang, E.K.; Louie, S.G. Structural properties and quasiparticle band structure of zirconia. *Phys. Rev. B Condens. Matter* **1998**, *57*, 7027–7036. [[CrossRef](#)]
22. Pongchan, G.; Ksapabutr, B.; Panapoy, M. One-step synthesis of flower-like carbon-doped ZrO<sub>2</sub> for visible-light-responsive photocatalyst. *Mater. Des.* **2016**, *89*, 137–145. [[CrossRef](#)]
23. Soares, M.R.N. Development of Zirconia Based Phosphors for Application in Lighting and as Luminescent Bioprobes. Ph.D. Thesis, University of Aveiro, Aveiro, Portugal, 2016. Available online: <https://ria.ua.pt/handle/10773/15884> (accessed on 21 July 2022).

24. Nova, C.V.; Reis, K.A.; Pinheiro, A.L.; Dalmaschio, C.J.; Chiquito, A.J.; Teodoro, M.D.; Rodrigues, A.D.; Longo, E.; Pontes, F.M. Synthesis, characterization, photocatalytic, and antimicrobial activity of ZrO<sub>2</sub> nanoparticles and Ag@ZrO<sub>2</sub> nanocomposite prepared by the advanced oxidative process/hydrothermal route. *J. Sol-Gel Sci. Technol.* **2021**, *98*, 113–126. [[CrossRef](#)]
25. Stolzenburg, P.; Freytag, A.; Bigall, N.C.; Garnweitner, G. Fractal growth of ZrO<sub>2</sub> nanoparticles induced by synthesis conditions. *CrystEngComm* **2016**, *18*, 8396–8405. [[CrossRef](#)]
26. Rafiq Hussain Siddiqui, M.; Ibrahim Al-Wassil, A.; Mohammed Al-Otaibi, A.; Mohamad Mahfouz, R. Effects of Precursor on the Morphology and Size of ZrO<sub>2</sub> Nanoparticles, Synthesized by Sol-gel Method in Non-aqueous Medium. *Mater. Res.* **2012**, *15*, 986–989. [[CrossRef](#)]
27. Pang, Q.; Chen, H.; Wang, X.; Wang, T.; Wang, D.; Feng, S.; Lu, H.; Li, Q. Field Effect Transistors Based on In Situ Fabricated Graphene Scaffold–ZrO<sub>2</sub> Nanofilms. *Adv. Electron. Mater.* **2018**, *4*, 1–6. [[CrossRef](#)]
28. Sani, E.; Sciti, D.; Capiiani, C.; Silvestroni, L. Colored zirconia with high absorbance and solar selectivity. *Scr. Mater.* **2020**, *186*, 147–151. [[CrossRef](#)]
29. Sani, E.; Mercatelli, L.; Sans, J.L.; Sciti, D. Optical properties of black and white ZrO<sub>2</sub> for solar receiver applications. *Sol. Energy Mater. Sol. Cells* **2015**, *140*, 477–482. [[CrossRef](#)]
30. Silvestroni, L.; Capiiani, C.; Sciti, D.; Sani, E. Coloring zirconium oxide for novel energy saving industrial applications. *Renew. Energy* **2022**, *190*, 223–231. [[CrossRef](#)]
31. Silva, J.P.B.; Silva, J.M.B.; Sekhar, K.C.; Palneedi, H.; Istrate, M.C.; Negrea, R.F.; Ghica, C.; Chahboun, A.; Pereira, M.; Gomes, M.J.M. Energy storage performance of ferroelectric ZrO<sub>2</sub> film capacitors: Effect of HfO<sub>2</sub>:Al<sub>2</sub>O<sub>3</sub> dielectric insert layer. *J. Mater. Chem. A* **2020**, *8*, 14171–14177. [[CrossRef](#)]
32. Pešić, M.; Hoffmann, M.; Richter, C.; Mikolajick, T.; Schroeder, U. Nonvolatile Random Access Memory and Energy Storage Based on Antiferroelectric Like Hysteresis in ZrO<sub>2</sub>. *Adv. Funct. Mater.* **2016**, *26*, 7486–7494. [[CrossRef](#)]
33. Wang, Y.; Wang, Y.; Zeng, H.; Wei, X. Ultra-high energy storage density of transparent capacitors based on linear dielectric ZrO<sub>2</sub> thin films with the thickness scaled up to hundreds nanometers. *Appl. Phys. Lett.* **2022**, *120*, 023904. [[CrossRef](#)]
34. Nunes, D.; Vilarigues, M.; Correia, J.B.; Carvalho, P.A. Nickel–carbon nanocomposites: Synthesis, structural changes and strengthening mechanisms. *Acta Mater.* **2012**, *60*, 737–747. [[CrossRef](#)]
35. Vidya, Y.S.; Anantharaju, K.S.; Nagabhushana, H.; Sharma, S.C.; Nagaswarupa, H.P.; Prashantha, S.C.; Shivakumara, C. Danithkumar Combustion synthesized tetragonal ZrO<sub>2</sub>: Eu<sup>3+</sup> nanophosphors: Structural and photoluminescence studies. *Spectrochim. Acta Part A Mol. Biomol. Spectrosc.* **2015**, *135*, 241–251. [[CrossRef](#)] [[PubMed](#)]
36. Bumajdad, A.; Nazeer, A.A.; Al Sagheer, F.; Nahar, S.; Zaki, M.I. Controlled Synthesis of ZrO<sub>2</sub> Nanoparticles with Tailored Size, Morphology and Crystal Phases via Organic/Inorganic Hybrid Films. *Sci. Rep.* **2018**, *8*, 3695. [[CrossRef](#)] [[PubMed](#)]
37. Jiang, C.; Wang, F.; Wu, N.; Liu, X. Up- and down-conversion cubic zirconia and hafnia nanobelts. *Adv. Mater.* **2008**, *20*, 4826–4829. [[CrossRef](#)]
38. Cao, H.; Qiu, X.; Luo, B.; Liang, Y.; Zhang, Y.; Tan, R.; Zhao, M.; Zhu, Q. Synthesis and Room-Temperature Ultraviolet Photoluminescence Properties of Zirconia Nanowires. *Adv. Funct. Mater.* **2004**, *14*, 1–4. [[CrossRef](#)]
39. Stepień, M.; Handzlik, P.; Fitzner, K. Synthesis of ZrO<sub>2</sub> nanotubes in inorganic and organic electrolytes by anodic oxidation of zirconium. *J. Solid State Electrochem.* **2014**, *18*, 3081–3090. [[CrossRef](#)]
40. Mangla, O.; Roy, S. Monoclinic Zirconium Oxide Nanostructures Having Tunable Band Gap Synthesized under Extremely Non-Equilibrium Plasma Conditions. *Proceedings* **2019**, *3*, 10. [[CrossRef](#)]
41. Yue, M.; Cui, M.; Zhang, N.; Long, Z.; Huang, X. Characterization of CeO<sub>2</sub>-ZrO<sub>2</sub> mixed oxides prepared by two different co-precipitation methods. *J. Rare Earths* **2013**, *31*, 251–256. [[CrossRef](#)]
42. Lim, H.S.; Ahmad, A.; Hamzah, H. Synthesis of zirconium oxide nanoparticle by sol-gel technique. *AIP Conf. Proc.* **2013**, *1571*, 812. [[CrossRef](#)]
43. Zinatloo-Ajabshir, S.; Salavati-Niasari, M. Synthesis of pure nanocrystalline ZrO<sub>2</sub> via a simple sonochemical-assisted route. *J. Ind. Eng. Chem.* **2014**, *20*, 3313–3319. [[CrossRef](#)]
44. Liang, J.; Jiang, X.; Liu, G.; Deng, Z.; Zhuang, J.; Li, F.; Li, Y. Characterization and synthesis of pure ZrO<sub>2</sub> nanopowders via sonochemical method. *Mater. Res. Bull.* **2003**, *38*, 161–168. [[CrossRef](#)]
45. Beer, S.M.J.; Samelor, D.; Abdel Aal, A.; Etkorn, J.; Rogalla, D.; Turgambaeva, A.E.; Esvan, J.; Kostka, A.; Vahlas, C.; Devi, A. Direct liquid injection chemical vapor deposition of ZrO<sub>2</sub> films from a heteroleptic Zr precursor: Interplay between film characteristics and corrosion protection of stainless steel. *J. Mater. Res. Technol.* **2021**, *13*, 1599–1614. [[CrossRef](#)]
46. Chang, Y.; Li, X. Bin Preparation of ZrO<sub>2</sub> spherical nanometer powders by emulsion processing route. *Trans. Nonferrous Met. Soc. China* **2006**, *16*, s332–s336. [[CrossRef](#)]
47. Lee, M.H.; Tai, C.Y.; Lu, C.H. Synthesis of spherical zirconia by reverse emulsion precipitation. *Korean J. Chem. Eng.* **1999**, *16*, 818–822. [[CrossRef](#)]
48. Zhao, N.; Pan, D.; Nie, W.; Ji, X. Two-phase synthesis of shape-controlled colloidal zirconia nanocrystals and their characterization. *J. Am. Chem. Soc.* **2006**, *128*, 10118–10124. [[CrossRef](#)]
49. Guo, M.; Wang, G.; Zhao, Y.; Li, H.; Tang, K.; Zhao, Y.; Burgess, K. Preparation of Nano-ZrO<sub>2</sub> powder via a microwave-assisted hydrothermal method. *Ceram. Int.* **2021**, *47*, 12425–12432. [[CrossRef](#)]

50. Gonell, F.; Portehault, D.; Julián-López, B.; Vallé, K.; Sanchez, C.; Corma, A. One step microwave-assisted synthesis of nanocrystalline  $\text{WO}_x\text{-ZrO}_2$  acid catalysts. *Catal. Sci. Technol.* **2016**, *6*, 8257–8267. [CrossRef]
51. Bondioli, F.; Bonamartini Corradi, A.; Ferrari, A.M.; Leonelli, C. Synthesis of Zirconia Nanoparticles in a Continuous-Flow Microwave Reactor. *J. Am. Ceram. Soc.* **2008**, *91*, 3746–3748. [CrossRef]
52. Kim, J.R.; Myeong, W.J.; Ihm, S.K. Characteristics of  $\text{CeO}_2\text{-ZrO}_2$  mixed oxide prepared by continuous hydrothermal synthesis in supercritical water as support of Rh catalyst for catalytic reduction of NO by CO. *J. Catal.* **2009**, *263*, 123–133. [CrossRef]
53. Li, Q.; Liu, L.; Wang, Z.; Wang, X. Continuous Hydrothermal Flow Synthesis and Characterization of  $\text{ZrO}_2$  Nanoparticles Doped with  $\text{CeO}_2$  in Supercritical Water. *Nanomaterials* **2022**, *12*, 668. [CrossRef]
54. Hobbs, H.; Briddon, S.; Lester, E. The synthesis and fluorescent properties of nanoparticulate  $\text{ZrO}_2$  doped with Eu using continuous hydrothermal synthesis. *Green Chem.* **2009**, *11*, 484–491. [CrossRef]
55. Dudnik, E.V. Modern methods for hydrothermal synthesis of  $\text{ZrO}_2$ -based nanocrystalline powders. *Powder Metall. Met. Ceram.* **2009**, *48*, 238–248. [CrossRef]
56. Liu, L.; Wang, S.; Zhang, B.; Jiang, G.; Yang, J. Supercritical hydrothermal synthesis of nano- $\text{ZrO}_2$ : Influence of technological parameters and mechanism. *J. Alloy. Compd.* **2022**, *898*, 16287. [CrossRef]
57. Darr, J.A.; Zhang, J.; Makwana, N.M.; Weng, X. Continuous Hydrothermal Synthesis of Inorganic Nanoparticles: Applications and Future Directions. *Chem. Rev.* **2017**, *117*, 11125–11238. [CrossRef]
58. Ponkumar, S.; Janaki, K.; Prakashbabu, D.; B Ramalingam, H.; Munirathnam, K.; Hari Krishna, R. Solution Combustion Synthesis of  $\text{ZrO}_2\text{:Tb}^{3+}$  Nanophosphors Viable for WLEDs. *Mater. Today Proc.* **2018**, *5*, 10717–10721. [CrossRef]
59. Samantaray, S.; Mishra, B.G.; Pradhan, D.K.; Hota, G. Solution combustion synthesis and physicochemical characterization of  $\text{ZrO}_2\text{-MoO}_3$  nanocomposite oxides prepared using different fuels. *Ceram. Int.* **2011**, *37*, 3101–3108. [CrossRef]
60. Purohit, R.D.; Saha, S.; Tyagi, A.K. Combustion synthesis of nanocrystalline  $\text{ZrO}_2$  powder: XRD, Raman spectroscopy and TEM studies. *Mater. Sci. Eng. B Solid-State Mater. Adv. Technol.* **2006**, *130*, 57–60. [CrossRef]
61. Carlos, E.; Martins, R.; Fortunato, E.; Branquinho, R. Solution Combustion Synthesis: Towards a Sustainable Approach for Metal Oxides. *Chem.—A Eur. J.* **2020**, *26*, 9099–9125. [CrossRef]
62. Branquinho, R.; Santa, A.; Carlos, E.; Salgueiro, D.; Barquinha, P.; Martins, R.; Fortunato, E. Solution Combustion Synthesis: Applications in Oxide Electronics. In *Developments in Combustion Technology*; IntechOpen: London, UK, 2016; ISBN 978-953-51-2669-0.
63. Moreira, M.; Carlos, E.; Dias, C.; Deuermeier, J.; Pereira, M.; Barquinha, P.; Branquinho, R.; Martins, R.; Fortunato, E. Tailoring IGZO Composition for Enhanced Fully Solution-Based Thin Film Transistors. *Nanomaterials* **2019**, *9*, 1273. [CrossRef]
64. Merten, D.; Broekaert, J.A.C.; Brandt, R.; Jakubowski, N. Analysis of  $\text{ZrO}_2$  powders by microwave assisted digestion at high pressure and ICP atomic spectrometry. *J. Anal. At. Spectrom.* **1999**, *14*, 1093–1098. [CrossRef]
65. Iqbal, Z.; Sadiq, S.; Sadiq, M.; Khan, I.; Saeed, K. Effect of Microwave Irradiation on the Catalytic Activity of Tetragonal Zirconia: Selective Hydrogenation of Aldehyde. *Arab. J. Sci. Eng.* **2021**, *47*, 5841–5848. [CrossRef]
66. Srikalyani, C.H.; Sultana, S. Microwave Synthesis of  $\text{ZrO}_2$  Nanoparticles and its Reinforcement in Geo-Polymer gel. *Int. J. ChemTech Res.* **2017**, *10*, 1–6.
67. Goharshadi, E.K.; Hadadian, M. Effect of calcination temperature on structural, vibrational, optical, and rheological properties of zirconia nanoparticles. *Ceram. Int.* **2012**, *38*, 1771–1777. [CrossRef]
68. Padovini, D.S.S.; Pontes, D.S.L.; Dalmaschio, C.J.; Pontes, F.M.; Longo, E. Facile synthesis and characterization of  $\text{ZrO}_2$  nanoparticles prepared by the AOP/hydrothermal route. *RSC Adv.* **2014**, *4*, 38484–38490. [CrossRef]
69. Liu, G.X.; Liu, A.; Meng, Y.; Shan, F.K.; Shin, B.C.; Lee, W.J.; Cho, C.R. Annealing dependence of solution-processed ultra-thin  $\text{ZrO}_x$  films for gate dielectric applications. *J. Nanosci. Nanotechnol.* **2015**, *15*, 2185–2191. [CrossRef]
70. Valle, H.R.L. Effect of Eco-Friendly Solvents in Solution-Based  $\text{ZrO}_x$  Dielectrics. Master's Thesis, FCT-UNL, Caparica, Portugal, 2019. Available online: <https://run.unl.pt/handle/10362/91651> (accessed on 21 July 2022).
71. Seon, J.B.; Cho, N.K.; Yoo, G.; Kim, Y.S.; Char, K. Solution-processed amorphous  $\text{ZrO}_2$  gate dielectric films synthesized by a non-hydrolytic sol-gel route. *RSC Adv.* **2018**, *8*, 39115–39119. [CrossRef]
72. Gong, Y.; Zhao, K.; He, H.; Cai, W.; Tang, N.; Ning, H.; Wu, S.; Gao, J.; Zhou, G.; Lu, X.; et al. Solution processable high quality  $\text{ZrO}_2$  dielectric films for low operation voltage and flexible organic thin film transistor applications. *J. Phys. D Appl. Phys.* **2018**, *51*, 115105. [CrossRef]
73. Wang, S.; Xia, G. A facile low-cost preparation of high- $k$   $\text{ZrO}_2$  dielectric films for superior thin-film transistors. *Ceram. Int.* **2019**, *45*, 23666–23672. [CrossRef]
74. Jung, S.H.; Han, H.S.; Kim, Y.B.; Kim, D.S.; Deshpande, N.G.; Oh, S.J.; Choi, J.H.; Cho, H.K. Toward ultraviolet solution processed  $\text{ZrO}_x$ /IZO transistors with top-gate and dual-gate operation: Selection of solvents, precursors, stabilizers, and additive elements. *J. Alloy. Compd.* **2020**, *847*, 156431. [CrossRef]
75. Luo, C.; Huang, T.; Li, C.; Zhang, Y.; Zou, Z.; Li, Y.; Tao, R.; Gao, J.; Zhou, G.; Lu, X.; et al. Enhancement of electrical properties of solution-processed oxide thin film transistors using  $\text{ZrO}_2$  gate dielectrics deposited by an oxygen-doped solution. *J. Phys. D Appl. Phys.* **2021**, *54*, 125101. [CrossRef]
76. Aminipoya, H.; Ghomi, A.B.; Niazi, A. Comparative synthesis of  $\text{ZrO}_2$  nanoparticles by green and co-precipitation methods: The effect of template on structure. *Int. J. Nano Dimens* **2021**, *12*, 59–66.

77. Ji, P.; Wang, Z.; Shang, X.; Zhang, Y.; Liu, Y.; Mao, Z.; Shi, X. Direct observation of enhanced Raman scattering on nano-sized ZrO<sub>2</sub> substrate: Charge-transfer contribution. *Front. Chem.* **2019**, *7*, 245. [CrossRef] [PubMed]
78. Soares, M.R.N.; Nico, C.; Peres, M.; Ferreira, N.; Fernandes, A.J.S.; Monteiro, T.; Costa, F.M. Structural and optical properties of europium doped zirconia single crystals fibers grown by laser floating zone. *J. Appl. Phys.* **2011**, *109*, 013516. [CrossRef]
79. Merle, T.; Guinebretiere, R.; Mirgorodsky, A.; Quintard, P. Polarized Raman spectra of tetragonal pure ZrO<sub>2</sub> measured on epitaxial films. *Phys. Rev. B—Condens. Matter Mater. Phys.* **2002**, *65*, 1443021–1443026. [CrossRef]
80. Fernandez Lopez, E.; Sanchez Escribano, V.; Panizza, M.; Carnasciali, M.M.; Busca, G. Vibrational and electronic spectroscopic properties of zirconia powders. *J. Mater. Chem.* **2001**, *11*, 1891–1897. [CrossRef]
81. Ding, S.; Zhao, J.; Yu, Q. Effect of zirconia polymorph on vapor-phase ketonization of propionic acid. *Catalysts* **2019**, *9*, 768. [CrossRef]
82. Gopal, R.; Jain, J.; Goyal, A.; Gupta, D.K.; Nagar, M. Formation of nano-sized cubic zirconia by aqueous sol–gel route. *J. Aust. Ceram. Soc.* **2018**, *54*, 691–700. [CrossRef]
83. Basahel, S.N.; Ali, T.T.; Mokhtar, M.; Narasimharao, K. Influence of crystal structure of nanosized ZrO<sub>2</sub> on photocatalytic degradation of methyl orange. *Nanoscale Res. Lett.* **2015**, *10*, 73. [CrossRef]
84. Lopes, D. Low-Cost Upconversion Nanomaterials for Anti-Counterfeiting Solutions. Master's Thesis, FCT-UNL, Caparica, Portugal, 2020. Available online: <https://run.unl.pt/handle/10362/113701> (accessed on 22 July 2022).
85. Prasad, K.; Pinjari, D.V.; Pandit, A.B.; Mhaske, S.T. Synthesis of zirconium dioxide by ultrasound assisted precipitation: Effect of calcination temperature. *Ultrason. Sonochemistry* **2011**, *18*, 1128–1137. [CrossRef]
86. Carvalho, J.M.; Rodrigues, L.C.V.; Felinto, M.C.F.C.; Nunes, L.A.O.; Hölsä, J.; Brito, H.F. Structure–property relationship of luminescent zirconia nanomaterials obtained by sol–gel method. *J. Mater. Sci.* **2015**, *50*, 873–881. [CrossRef]
87. Kiisk, V.; Puust, L.; Utt, K.; Maaros, A.; Mändar, H.; Viviani, E.; Piccinelli, F.; Saar, R.; Joost, U.; Sildos, I. Photo-, thermo- and optically stimulated luminescence of monoclinic zirconia. *J. Lumin.* **2016**, *174*, 49–55. [CrossRef]
88. Lokesha, H.S.; Nagabhushana, K.R.; Singh, F.; Tatumi, S.H.; Prinsloo, A.R.E.; Sheppard, C.J. Unraveling the Charge State of Oxygen Vacancies in Monoclinic ZrO<sub>2</sub> and Spectroscopic Properties of ZrO<sub>2</sub>:Sm<sup>3+</sup> Phosphor. *J. Phys. Chem. C* **2021**, *125*, 27106–27117. [CrossRef]
89. Perevalov, T.V.; Gulyaev, D.V.; Aliev, V.S.; Zhuravlev, K.S.; Gritsenko, V.A.; Yelissev, A.P. The origin of 2.7 eV blue luminescence band in zirconium oxide. *J. Appl. Phys.* **2014**, *116*, 244109. [CrossRef]
90. Ashraf, S.; Irfan, M.; Kim, D.; Jang, J.-H.; Han, W.-T.; Jho, Y.-D. Optical influence of annealing in nano- and submicron-scale ZrO<sub>2</sub> powders. *Ceram. Int.* **2014**, *40*, 8513–8518. [CrossRef]
91. Jiang, H.; Gomez-Abal, R.I.; Rinke, P.; Scheffler, M. Electronic band structure of zirconia and hafnia polymorphs from the GW perspective. *Phys. Rev. B* **2010**, *81*, 085119. [CrossRef]
92. Gallino, F.; Di Valentin, C.; Pacchioni, G. Band gap engineering of bulk ZrO<sub>2</sub> by Ti doping. *Phys. Chem. Chem. Phys.* **2011**, *13*, 17667–17675. [CrossRef]
93. Li, J.; Meng, S.; Niu, J.; Lu, H. Electronic structures and optical properties of monoclinic ZrO<sub>2</sub> studied by first-principles local density approximation + *U* approach. *J. Adv. Ceram.* **2017**, *6*, 43–49. [CrossRef]
94. Singh, H.; Sunaina; Yadav, K.K.; Bajpai, V.K.; Jha, M. Tuning the bandgap of m-ZrO<sub>2</sub> by incorporation of copper nanoparticles into visible region for the treatment of organic pollutants. *Mater. Res. Bull.* **2020**, *123*, 110698. [CrossRef]
95. Teeparthi, S.R.; Awin, E.W.; Kumar, R. Dominating role of crystal structure over defect chemistry in black and white zirconia on visible light photocatalytic activity. *Sci. Rep.* **2018**, *8*, 5541. [CrossRef]
96. Sakfali, J.; Ben Chaabene, S.; Akkari, R.; Dappozze, F.; Berhault, G.; Guillard, C.; Saïd Zina, M. High photocatalytic activity of aerogel tetragonal and monoclinic ZrO<sub>2</sub> samples. *J. Photochem. Photobiol. A Chem.* **2022**, *430*, 113970. [CrossRef]
97. Smits, K.; Grigorjeva, L.; Millers, D.; Sarakovskis, A.; Grabis, J.; Lojkowski, W. Intrinsic defect related luminescence in ZrO<sub>2</sub>. *J. Lumin.* **2011**, *131*, 2058–2062. [CrossRef]
98. Sil, A.; Goldfine, E.A.; Huang, W.; Bedzyk, M.J.; Medvedeva, J.E.; Facchetti, A. Role of Fluoride Doping in Low-Temperature Combustion-Synthesized ZrO<sub>x</sub> Dielectric Films. *ACS Appl. Mater. Interfaces* **2022**, *14*, 12340–12349. [CrossRef]
99. Pradhan, S.; Mishra, B.G. Catalytic application of SO<sub>4</sub><sup>2-</sup>/Fe-ZrO<sub>2</sub> nanoparticles synthesized by a urea hydrolysis method for environmentally benign one pot synthesis of 1,8-dioxodecahydroacridines. *RSC Adv.* **2015**, *5*, 86179–86190. [CrossRef]
100. Cai, W.; Zhu, Z.; Wei, J.; Fang, Z.; Ning, H.; Zheng, Z.; Zhou, S.; Yao, R.; Peng, J.; Lu, X. A simple method for high-performance, solution-processed, amorphous ZrO<sub>2</sub> gate insulator TFT with a high concentration precursor. *Materials* **2017**, *10*, 972. [CrossRef] [PubMed]
101. Meng, Y.; Liu, G.; Liu, A.; Song, H.; Hou, Y.; Shin, B.; Shan, F. Low-temperature fabrication of high performance indium oxide thin film transistors. *RSC Adv.* **2015**, *5*, 37807–37813. [CrossRef]
102. Zhu, L.; He, G.; Lv, J.; Fortunato, E.; Martins, R. Fully solution-induced high performance indium oxide thin film transistors with ZrO<sub>x</sub> high-k gate dielectrics. *RSC Adv.* **2018**, *8*, 16788–16799. [CrossRef]
103. Lee, H.; Zhang, X.; Kim, J.W.; Kim, E.J.; Park, J. Investigation of the Electrical Characteristics of Bilayer ZnO/In<sub>2</sub>O<sub>3</sub> Thin-Film Transistors Fabricated by Solution Processing. *Materials* **2018**, *11*, 2103. [CrossRef]
104. Oluwabi, A.T.; Katerski, A.; Carlos, E.; Branquinho, R.; Mere, A.; Krunks, M.; Fortunato, E.; Pereira, L.; Oja Acik, I. Application of ultrasonic sprayed zirconium oxide dielectric in zinc tin oxide-based thin film transistor. *J. Mater. Chem. C* **2020**, *8*, 3730–3739. [CrossRef]

105. Zhu, C.; Liu, A.; Liu, G.; Jiang, G.; Meng, Y.; Fortunato, E.; Martins, R.; Shan, F. Low-temperature, nontoxic water-induced high-*k* zirconium oxide dielectrics for low-voltage, high-performance oxide thin-film transistors. *J. Mater. Chem. C* **2016**, *4*, 10715–10721. [[CrossRef](#)]
106. Boratto, M.H.; Congiu, M.; dos Santos, S.B.O.; Scalvi, L.V.A. Annealing temperature influence on sol-gel processed zirconium oxide thin films for electronic applications. *Ceram. Int.* **2018**, *44*, 10790–10796. [[CrossRef](#)]